DRONE MEASUREMENTS OF WETLAND SOILS & ROBOTIC MANIPULATION OF ENSEMBLES USING GLOBAL FORCES

by
Victor Montano Baez

A dissertation submitted to the Department of Mechanical Engineering,

Cullen College of Engineering

in partial fulfillment of the requirements for the degree of

MASTER OF SCIENCES
in Aerospace Engineering

Chair of Committee: Dr. Karolos Grigoriadis

Committee Member: Dr. Aaron T. Becker

Committee Member: Dr. Matthew A. Franchek

Committee Member: Dr. Navid Jafari

University of Houston
May 2021

PREFACE

This thesis presents *"Assessment of Soil Strength using a Robotically Deployed and Retrieved Penetrometer,"* published in *2020 IEEE/RSJ International Conference on Intelligent Robots and Systems (IROS 2020)* [1] and *"Wetland Soil Strength Tester and Core Sampler Using a Drone,"* published in *2021 IEEE/RSJ International Conference on Intelligent Robots and Systems (ICRA 2021)* [2]. This thesis also presents parts of work from *"Coordinated Particle Relocation Using Finite Static Friction with Boundary Walls,"* published in *ICRA 2020* [3] and *"Aggregation and localization of simple robots in curved environments,"* published in *ICRA 2020* [4].

ACKNOWLEDGEMENTS

Dr. Aaron T. Becker, thank you so much for being my thesis advisor, an amazing role model, and always being there for me. Thank you for showing me how much fun research could be; if it weren't for you, I would not have wanted to come back to graduate school for more research—it's been incredible fun and if I had the opportunity, I would do it all over again. It's been a true honor to work for one of my greatest inspirations.

I thank the members of my thesis committee, Dr. Karolos Grigoriadis, Dr. Matthew A. Franchek and Dr. Navid Jafari. Dr. G and Dr. Franchek, your undergraduate courses were my favorite and they inspired my graduate course focus in control theory. Dr. G, thank you for taking an interest in our work and keeping up with me and the research I was part of throughout graduate school. Dr. Franchek, every moment I got to spend with you was a real treat, and I'll never forget all of the inspirational stories you've shared with me. Dr. Jafari, it was an honor that you recognized our previous research and came to us to team up and develop new technologies with you.

Ami Shah, Shreyas Poyrekar, Srikanth Kandanuru Venkata Sudarshan, Samuel Akinwande, Marcos Ibarra, Yusef Haikal, Saurahb Sogi, Dr. Arne Schmidt, Rachel A. Moan, Dr. Craig Glennie, Darren L. Hauser, Abhinav Singhani, Dr. Sándor Fekete, Dr. Jason O'Kane, Dr. Navid H. Jafari, and Dr. Aaron T. Becker; without you guys, this work would not be possible, and it was a true pleasure to work with all of you.

To all the members of Dr. Becker's lab, it was the colossal support of your friendship that held me up through all of my struggles, and I cannot thank you enough.

Dr. Alan Wiederhold, the very start of my academic journey began in your trigonometry course. You showed me that the joys of solving problems are independent of application or utility. To this day, the mindset you fostered helps me solve problems beyond the many branches of mathematics you taught me.

Finally, I thank my wonderful mother for all of her support and loving me unconditionally. Mom, you're the hardest working person I know and without a doubt the best mother on this planet.

ABSTRACT

This thesis covers two applications of robotics. The first section explores the use of drones for measuring properties of soil. Technologies in this section were developed to aid coastal scientists and geotechnical engineers in the structural analysis of wetland environments. These include ballistic sensors inspired by free-fall penetrometers that were designed to be deployed and retrieved by drones. They exploit the deceleration experienced upon impacting moist soils to infer on soil resistance. In later developments, these sensors are made to also retrieve soil samples while simultaneously performing soil strength tests. Experiments are performed in simulated environments to demonstrate the use of the developed sensors for collecting soil strength parameters, retrieving soil samples, and also to study the effort required for drone retrieval within the context of pull forces. Overcoming some of the challenges associated with retrieval are discussed, and some solutions are presented.

The second section examines using global forces to move large numbers of particles at the same time into desired goal positions. This process for manipulation uses the properties of boundary walls to shape the ensemble, including the shape of the walls and friction between the boundary and the particles. Experiments that verify theories on this style of manipulation are presented, along with tools that simplify hardware experiments of this variety.

TABLE OF CONTENTS

LIST OF FIGURES

1 Introduction

As novelty in the field of robotics persists, expectations of its future make a stale comparison to the marvels of present academic pursuits. Engineers are coming up with ways to steer tiny robots through blood vessels to drill through clots [5, 6]. Wielding superhuman strength with exoskeletons will soon no longer be restricted to adults [7]. Authors of [8,9] are working on self-assembling structures and they are nearly ready for the live-action version of Disney's Big Hero 6. Soon, even facilities in space will build themselves [10]. Participating species may have conflicting interpretations of [11], where drones are being used to conclude populations of mosquitoes. In [12], roboticists are studying the adversarial relationship between an army of drones and subjects with firearms. Perspective tends to dictate whether a swarm of flying robots is terrifying or inviting. This thesis begins with an application of drones in a warm coastal setting aimed to relieve some of the labors in sediment analysis.

1.1 Thesis Outline

Chapter 2 presents a free-fall penetrometer dart designed to be deployed by a UAV into coastal soils for structural analysis along with experiments where the dart is used to collect soil strength measurements of a simulated marsh environment. Chapter 3 presents work from [2], a paper that continues the development of the dart developed in [1], presented in Chapter 2. In this work, the spike of the dart is modified so that it can retrieve soil samples. The effects of retrieving soil samples on the strength measurements are also discussed. Chapter 4 is all about retrieval. The force required of a drone when retrieving a planted dart is measured using carefully designed experiments. A mechanism that was designed to deploy and retrieve the same sensing dart multiple times for repeated testing is presented. Chapter 4 concludes with a final demonstration of successful repeated testing using the technologies presented. Chapter 5 presents tools that were designed to implement and experimentally verify theories in [3] and [4] on manipulating the positions of multiple objects within a workspace under global inputs using their friction with their boundary. Chapter 6 offers suggestions for future work.

2 A UAV-Deployed FFP for Wetland Soils

The sensing dart introduced here was designed as part of an initiative to develop a robotic system to deploy and retrieve sensors that would enable coastal scientists to measure data at a larger spatial scale and finer temporal scale than methods currently available. It is a free-fall penetrometer designed to be deployed by UAVs from sufficient heights to collect data that would aid in the structural analysis of wetland soils. Experiments were performed where the dart was dropped into different soils to demonstrate its capabilities. Work in this chapter is from [1].

Figure 1: Aerial view of a salt marsh off the coast of Louisiana

2.1 Coastal Wetlands

Salt marshes are wetlands flooded periodically by tides and dominated by grasses (Figure 1). They occupy the land-sea boundary and survive rising seas by accreting soil. However, the ability of salt marshes to accrete soil is rate-limited, causing coastal erosion due to sea-level rise [13]. Knowledge gaps limit predictive understanding of the interactions between plants, the soil matrix, and the dynamic physical environment that drives the response of salt marshes to climate change. In particular, coastal soils are exposed to daily wet/dry cycles from tides which presents monumental challenges for generating adequate datasets in support of accurate modeling of large-scale ecosystem behavior. Even when exposed at low tide, it is often not possible to sample soils within a few meters from the marsh edge by boat or on foot without destroying the physical substrate and contaminating the chemistry. Rapid assessments of wetland conditions use hydrology, hydric soils, and wetland biotic communities to understand changes in wetland function, ecological integrity, and mitigation success. However, the soil assessment components are the least developed [14].

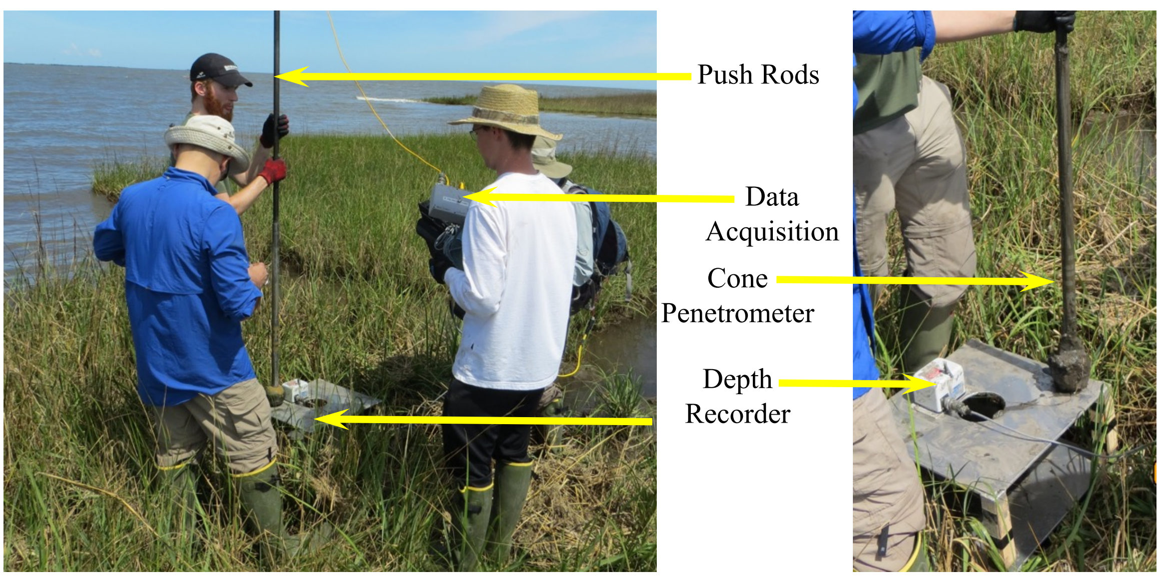

Figure 2: Manually obtaining CPT data from a wetland requires multiple people, and trekking through sensitive features. The method presented in this paper could reduce the impact on the wetlands, and simplify the procedure

Cone penetrometer testing (CPT) is used in the field of geotechnical engineering to explore the subsurface stratigraphy and properties for the design of civil infrastructure [15].

The cone consists of a cylindrical rod with a conical tip that is driven into the ground at a constant rate. As it penetrates into soil, it measures the tip and sleeve resistance, along with pore-water pressure. These three variables are used together to identify soil types and estimate engineering properties, such as shear strength, stress history, and stiffness. The output of CPTs are used to design foundations for buildings, bridges, dams, levees, and other infrastructure. They are used to estimate the probability of liquefaction of sands and tailings dams during earthquakes. Recent innovations of CPT have involved applying the test to coastal and offshore environments. However, conducting CPTs in offshore environments is expensive because of the cost of mobilization in such extreme environments. Figure 2 shows civil engineering researchers performing a traditional CPT in a salt marsh off the coast of Louisiana.

2.2 FFP Designed for Aerial Deployment

2.2.1 Inspiration and Related Work

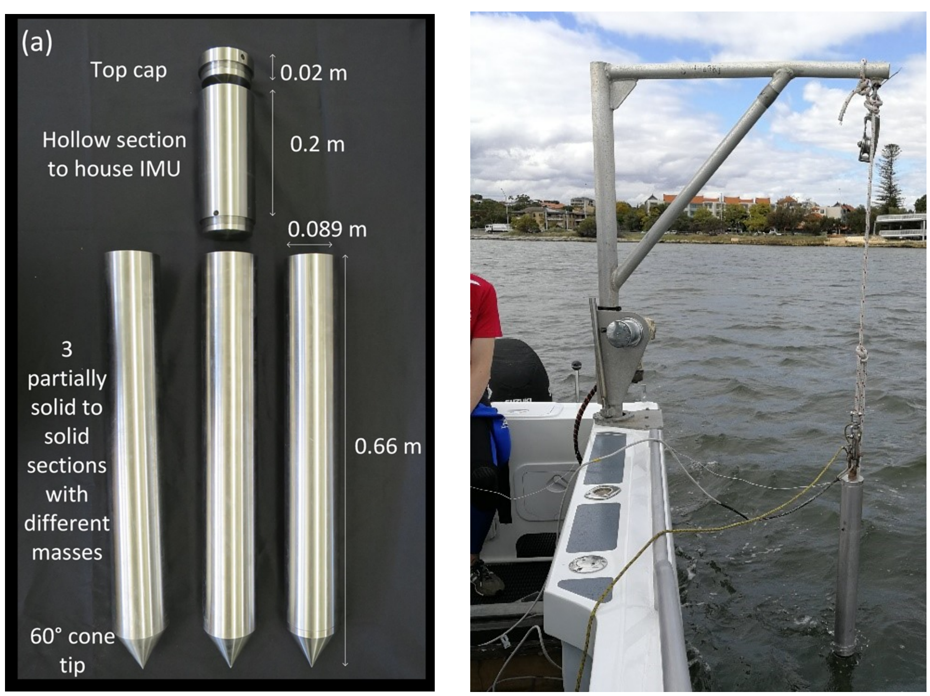

Figure 3: Offshore FFP design from the University of Western Australia in *"Development of a FreeFall Cone Penetrometer for Offshore Site Investigation"* by Conleth O'Loughlin, Shiaohuey Chow, and Vepulan Siritharan.

The sensing dart presented in this chapter is inspired by early free-falling penetrometers (FFPs) that were developed to measure the strength of seafloor sediments [16–19]. A example of an Offshore FFP developed by researchers from the University of Western Australia is shown in Figure 3. These studies involved dropping a heavy dart into the ocean such that it accelerates to a terminal velocity. The dart contains accelerometers to log the the deceleration as it impacts the ocean floor. The acceleration time history is double integrated to evaluate the depth of penetration into the seabed. The acceleration behavior was also used to estimate a quasi-static bearing capacity of the soil. Naxem et al. employed these for analyzing the dynamics of falling into uniform clay [20]. In [21], White et al. shows that the resistance of sandy soils measured by a high velocity FFP can be mapped to the resistance measured by a standard CPT.

Penetrating subaerial soil presents different challenges than in submarine environments because offshore deposits (cohesive and sands) are typically loosely deposited and soft. Accessing wetlands like salt marshes requires transportation by boat. Afterwards, traveling through these islands by foot is not easy because offshore deposits are typically loosely deposited and soft. Terrestrial soils such also vary significantly in particle size, consistency stiffness, and inclusion of roots or vegetation.

Soil indicators need to be developed to guide the efficacy of restoration projects, e.g., rebuilding drowning marshes using dredged sediment, improving drainage, and facilitating marsh migration. The addition of wetland soil data will strengthen salt marsh assessments because soils provide a record of both long and short-term changes in wetland conditions as a result of anthropogenic effects such as tidal restriction. Sensors designed to be deployed using UAVs would allow coastal scientists to survey larger areas easier. Deploying soil sensors from a distance would also preserve data that would otherwise be corrupted by human interaction with the condition of the environment associated with travel and transporting testing equipment.

2.2.2 The FFP Design

The dart is made up of three parts: a spike for penetrating soil, a shell containing the electronics, and a fin to stabilize orientation during free-fall. A 400g accelerometer (Sparkfun H3LIS331DL) connected to a Raspberry Pi Zero logged its impact deceleration. A switch inside the fin was used to turn the device off and on. All electronics were powered with a LiPo battery. All electronics were placed so the center of mass was on the y-axis of the accelerometer, which was aligned with the spike of the dart. This placement directs the impact force along the y-axis. Figure 4 shows the first design from [1]

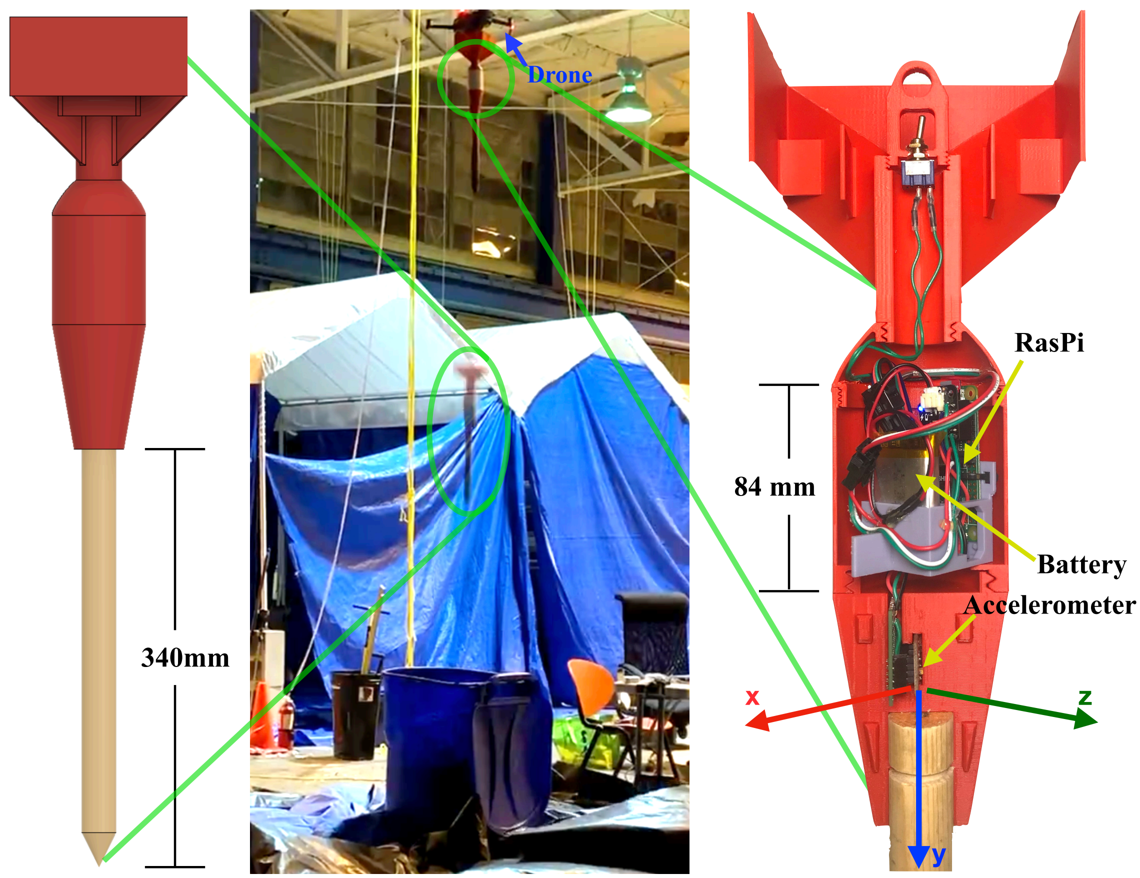

Figure 4: The drone-delivered soil penetrometer. On the left is a rendering of the dart. In the center is a photograph of a drone delivering a dart into a bin with mud. On the right is a physical cross-section of the dart showing the electronics.

2.3 Soil-Type Identification

To show that this FFP can effectively help coastal scientists in the structural analysis of wetland soils, the FFP was dropped into three different soil types and the impact deceleration was recorded. There were two goals for these drop test experiments: (1) to distinguish soil types using the deceleration data; and (2) to find suitable heights for a UAV to deploy the FFP. If soil types could be distinguished based on their impact deceleration profiles, this would imply that the FFP was effectively measuring the different soil resistances. At suitable deployment heights, there would be distinct differences in the deceleration profiles.

2.3.1 Drop Test Environment and Procedures

Three soils were chosen to represent a range of soil types found in a wetland. The first was *torpedo sand*, a naturally occurring course-grained sand and gravel mix. The second soil was *beach volleyball sand*, which consists of at least 80% 0.5 mm–1.0 mm particles. The third soil was saturated mud. The water content of each soil was estimated by measuring the change in mass when of a container of soil was dried at 100°C for 48 hours in a laboratory furnace. The water content of the torpedo soil was 7.46%, the volleyball sand was 11.68%, and the saturated mud was 30.5%. The three soils prior to drying them are shown in Figure 5.

Figure 5: The three soils used for the drop test experiments. Three 180 L recycling bins were filled with 125 L of each soil type for the drop tests.

The FFP was dropped into three 180 L (48 gallons) recycling bins that were filled with roughly 125 L (42 gallons) of each soil. The drops were performed manually using a pulley system to ensure consistent drop height and consistent vertical starting orientation of the dart. The three heights tested were 1.5 m, 2.5 m, and 3.5 m. Drop heights were measured from the tip of the dart spike to the top of the soil using a field measuring tape. In between each test, the soil was prepared using a hand cultivator, a shovel, and a garden claw to generate a uniform consistency of the soil mixture throughout the bin and re-level the top of the soil. An example of a drop test is shown in Figure 6. This figure is placed here, however, this is a photo from tests performed in [2], which is presented in Chapter 3.

2.3.2 Drop Test Results

Fig. 7 shows the impact deceleration for two sands and a cohesive mud. The acceleration starts at 0 g until the dart is dropped from the specific height, after which it accelerates through the duration of the drop height. At this point, the dart impacts the soil, begins to penetrate the soil, and decelerates until it comes to a rest. A labeled timeline of the impact event is shown in Fig. 7d. It should be noted that the data in Fig. 7d comes from work in [2], so the discrepancy in the resolution of the deceleration data in this figure and the other plots in Figure 7 is due to upgraded hardware in a second work [2] presented in Chapter 3.

The two sands in Figure 7(a) and 7(b) show a sharp peak at approximately 100 g, while Figure 7(c) shows a more shallow curve for the mud. In particular, the max acceleration experienced in the mud was 30 g. Sand is more stiff than clay so the behavior observed in Figure 7 indicates that higher accelerations correspond to higher strength soils. The narrow area under the curve for the sands indicates the dart comes to a rest more rapidly than with the mud. This further suggests that the dart penetrated less into the sands than mud. An observable difference in the acceleration time history was not evident until the highest drop, suggesting a minimum drop height is needed for successful penetration. Between the experiments, visual inspection shows that there is reproducibility of the tests. More variability is found in Figure 7(b) but the results are promising.

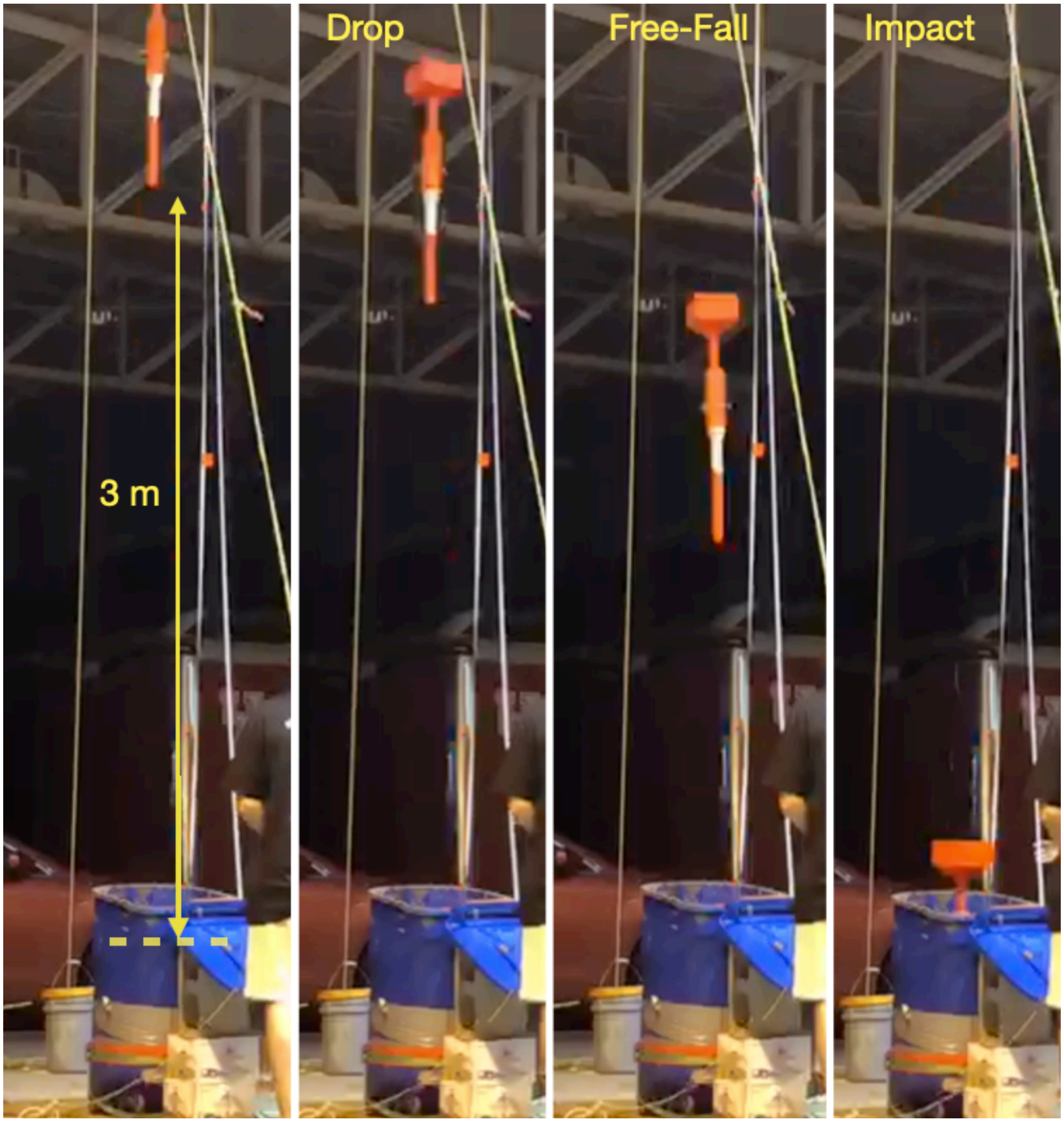

Figure 6: Example of drop test procedure. This Drop was from 3 m.

Figure 8 shows the change in acceleration for each specific soil type but plotted with consistent drop height. For a drop height of 1.5 m, the acceleration in mud reaches 8 g, whereas the torpedo sand and volleyball sand approach 12 g and 20 g, respectively. When the drop height increases to 2.5 m, the mud still shows the same behavior with a slight increase to 10 g. The sands now overlap (volleyball sand is slightly higher at 25 g compared to 20 g for torpedo sand) and suggest similar behavior and stiffness. The highest drop height of 3.7 m indicates a mud acceleration is 20 g and the torpedo sand approaches 80 g.

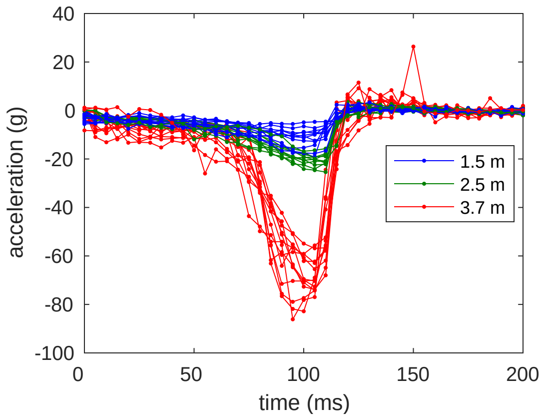

(a) Soil: Torpedo Sand

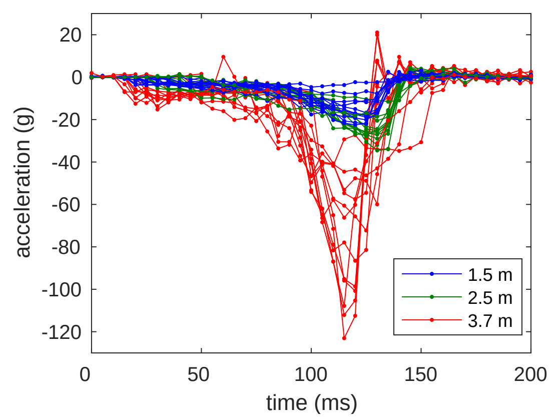

(b) Soil: Volleyball Sand.

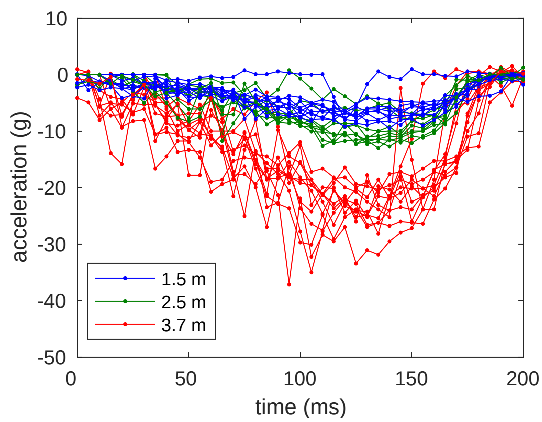

(c) Soil: saturated mud

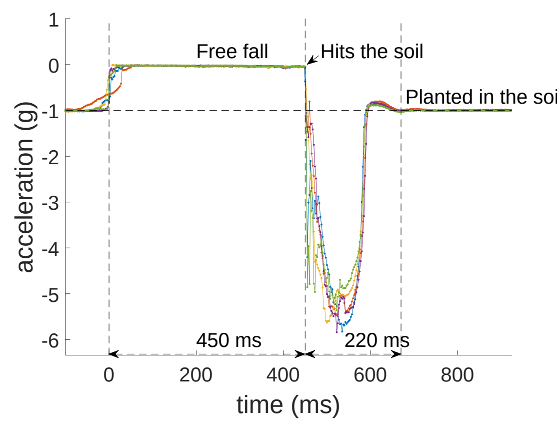

(d) Labeled Representative Timeline

Figure 7: Plot of the impact deceleration of our dart from three different drop heights into three soils.

The volleyball sand is evidently stiffer than the rest of the soils. This is further evident in Figure 9, which shows the penetration depth. In particular, the mean penetration depth was 110 mm for volleyball sand and 160 mm for torpedo sand, from a drop height of 1.5 m. For the sands, the penetration depth increases linearly with increasing drop height to 3.7 m. In contrast, the penetration depth for mud remains more constant over the drop heights. In these experiments, the penetration depth was measured manually, however in Section 3.2.3 it is shown that the penetration depth can be obtained by double integrating the impact deceleration data logged by the FFP.

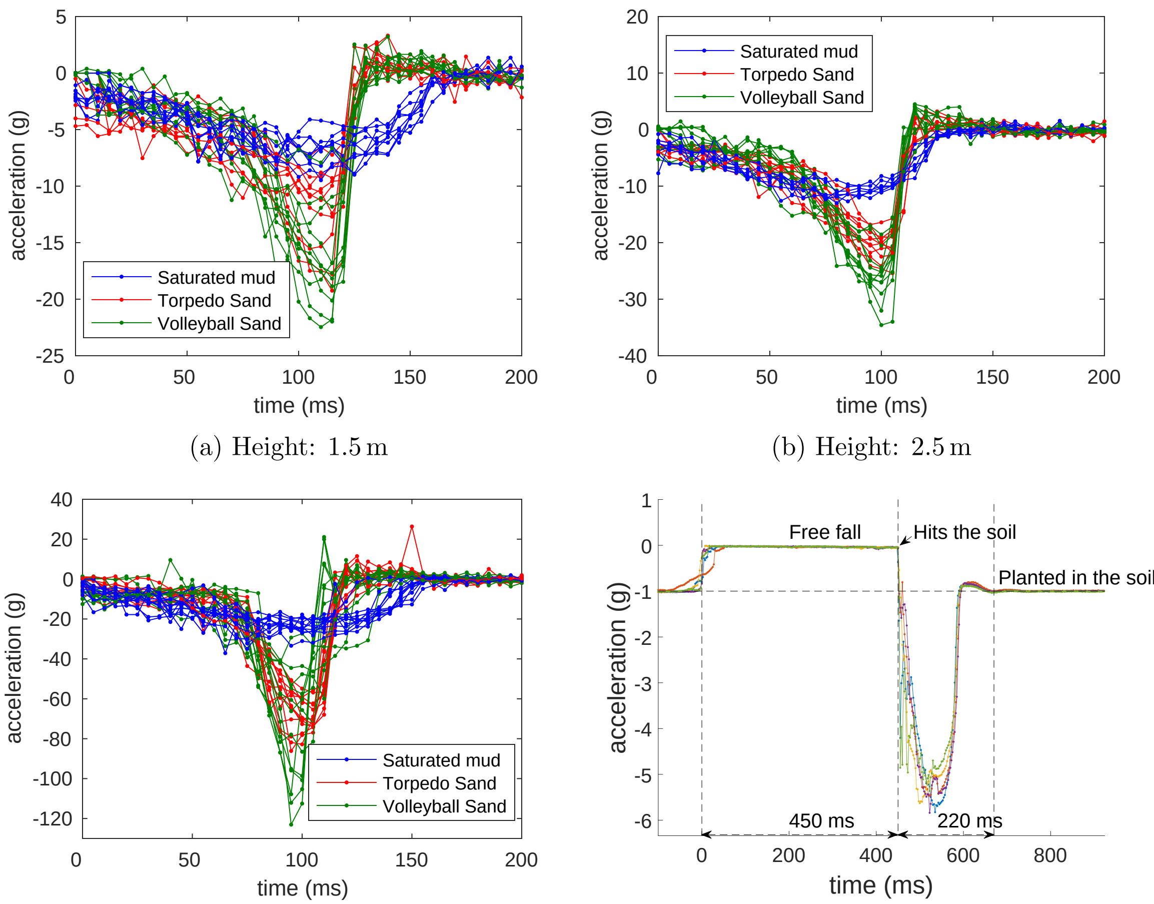

(a) Height: 1.5 m

(b) Height: 2.5 m

(c) Height: 3.7 m

(d) Labeled Representative Timeline

Figure 8: Distinguishing soil types using deceleration profiles of darts dropped from three different drop heights.

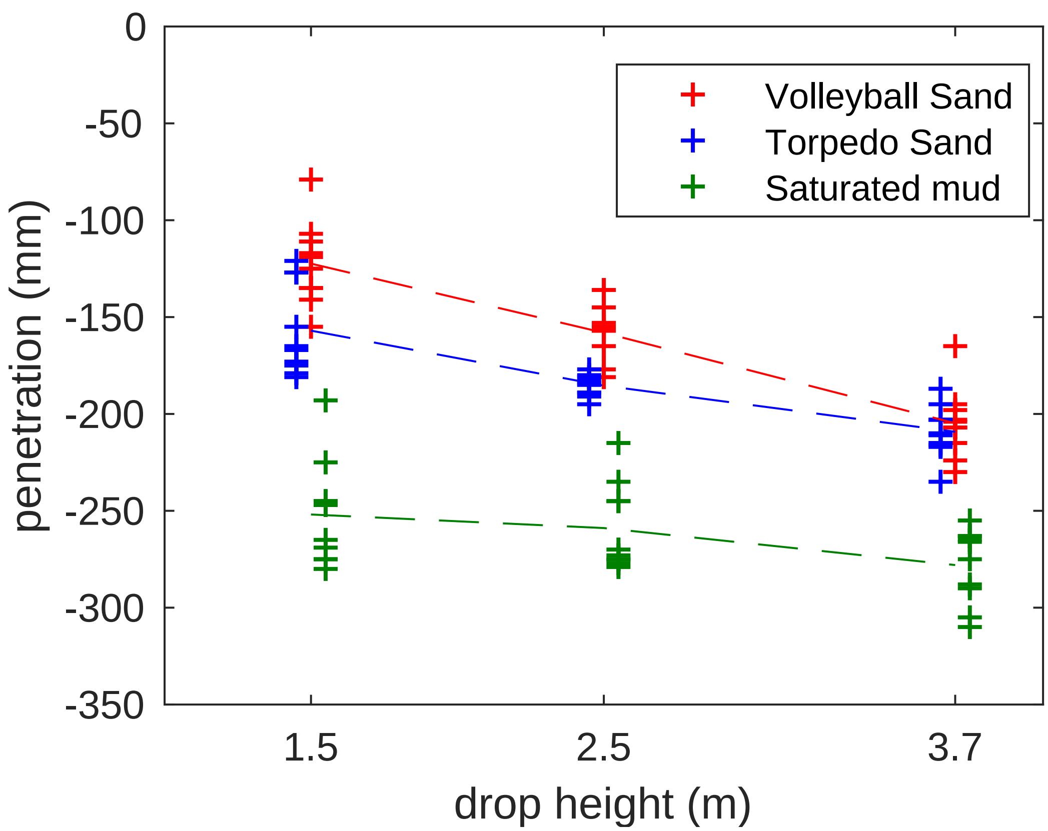

Figure 9: Penetration depth as a function of drop height and soil type. Penetration depth increases with drop height. The sands are similar, but the FFP penetrates roughly twice as deep into the saturated mud.

3 Collecting Soil Samples Using UAV-deployed FFPs

This chapter presents parts of [2], which continued on the development of the UAV deployed FFP dart from [1] presented in Chapter 2. The FFP spike tip was redesigned so that it could be used to retrieve soil samples while simultaneously performing soil-strength tests.

3.0.1 Motivation

The collection of soil physical-chemical data in wetland environments remains limited. This is primarily due to destructive sampling of soil cores caused by trekking through the soft substrate. Collecting soil cores on the coast is especially important because they provide valuable data on plant productivity, sediment accretionary dynamics, bulk densities, grain size distribution, and organic content [22–26]. *In situ* sensing approaches with the potential to rapidly evaluate wetland soil properties over large spatial scales represent an excellent opportunity to overcome these obstacles and improve predictive understanding of ecosystem-scale behavior. Moreover, a swarm of robots could enable multiple repeated *in situ* tests to rapidly evaluate soil properties, eliminating many drawbacks involved with access to ship time, invasive nature of field core sampling, and decreasing the overall number of core samples required.

Wetland vulnerability is commonly assessed using a three-tiered framework of landscape-scale assessment, rapid assessment protocols, and intensive biological and physiochemical measurements. All three methods involve manually trekking through the wetlands to collect cores for evaluating substrate biological and physical properties (see Figure 2). These laborious procedures are inefficient in terms of mobilizing equipment, productivity, paucity of data, and disturbance to the wetlands. Beyond the substantial time commitment required for analyzing field cores, measurement errors are pervasive due to variations in operation, type, and dimension of the coring device; compression of the sediment when taking the core and/or when extracting the core from the core tube; imprecise sectioning of the core into known volumes, variation in drying and furnace temperatures, and presence of salts that precipitate when the pore water is evaporated from the sample [26].

3.0.2 Related Work

Recent work involving UAV-deployed sensors include [27–30]. UAVs have been employed for collecting water samples [31–34], volcanic gas [35], and ice cores from icebergs [36]. Work in [27] fired sensor darts into trees, but these sensors are left embedded in the tree and cannot be reused by the drone unless they are manually removed. UAVs have been used to drill out and retrieve ice cores from icebergs in [36]. In [31], samples of water were taken using a UAV to lower a weighted, water-collecting sleeve 122 m into a body of water. To collect soil core samples, however, penetrating the soil is necessary, as shown in Figure 10 (on the left). Penetration requires the sensor dart to move very rapidly, which is accomplished by dropping it from a height. This paper examines a soil sampling technique that can embed a dart into soil, perform measurements during impact, collect soil samples, and can also be retracted to repeat the process in different locations.

There is also impressive research on using a drone-mounted auger to place sensors underground [37, 38]. This chapter is related to prior work using drones to deploy seismic sensors [28–30], only in this work the sensing takes place during the deployment, and the darts can then immediately be retrieved and redeployed to a new area.

3.1 Core-Sampling FFP Design

The goal of soil core sampling is to collect undisturbed soil samples. The left image in Fig. 10 is a Shelby tube sampler, a metal tube that is pushed into the soil and pulled out to remove a core of soil. This sampling method inspired improvements on the dart developed in Chapter 2 to add the ability to retrieve cores of soil.

The new dart features interchangeable tips for comparison experiments [2] . Two of the spikes, designed for outward core sampling, are hollow and have vents near the top for airflow so that soil would not be working against any air pressure during core sampling. The core-sampling tips are 450 mm long. This length is sufficient for dropping the FFP

Figure 10: On the left is a Shelby tube sampler. The hollow-core dart tips are shown on the right. These are modular, and can be extended to suit experimental needs.

from a 3 m height without burying the air vents. The inside diameters of the two hollow tips are 22 mm and 34 mm and the shell walls are 3 mm thick, giving an outer diameter of 40 mm. The last dart tip is a solid version of the larger diameter core-sampling tip, having a diameter of 40 mm. The electronics were also changed for greater sampling frequency of the impact deceleration. It contained a 16 g accelerometer (MPU6050), an SD card module, two 3.7 V LiPo batteries, and a switch. These were connected to an Arduino Mega (Atmega 2560), sampling the accelerometer at a rate of 400 Hz. The dart had a total weight of 850 g. It should be noted here that for the experiments in section 3.2, the mass of the dart was adjusted to keep a constant 850 g for each of the spikes tested. An illustration showing the full dart featuring the 34 mm hollow core-sampling tip and electronics is shown in Figure 11. The 22 mm and 34 mm diameter interchangeable dart tips are shown in Figure 10 (right image). These are shown here without their extensions.

3.2 Core-Sampling Experiments

Experiments here were performed to determine how effective the core-sampling version of the FFP dart is in retrieving soil samples, and how the diameter can influence the amount of soil collected. Also, deceleration profiles of darts with core-sampling spikes are

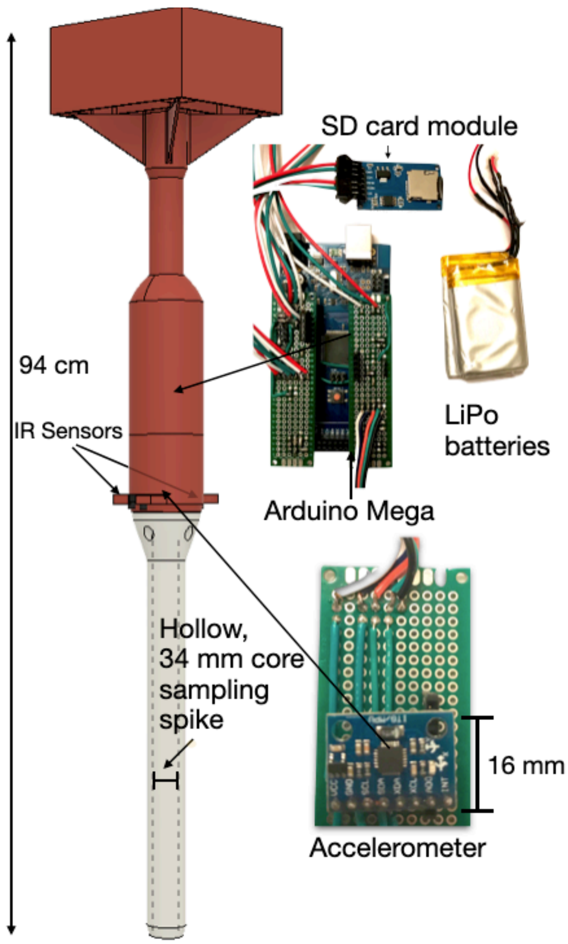

Figure 11: Rendering of dart used for drop testing featuring the hollow 34 mm inner diameter core-sampling spike. Inside it contains an SD card module, a 16 g accelerometer, and two 3.7 V LiPo batteries connected to an Arduino Mega.

compared with darts that have solid spikes to show how the hollow spikes influence the impact deceleration.

3.2.1 Enviornment and Procedures

The soil used in this study to simulate a wetland environment was produced by mixing water with fine-grained soils (silts and clays) until a mud consistency was reached to serve as a proxy for a marsh soil. The gravimetric water content of the resulting soil was 20%. A picture of our soil before and after adding water is shown in Figure 12.

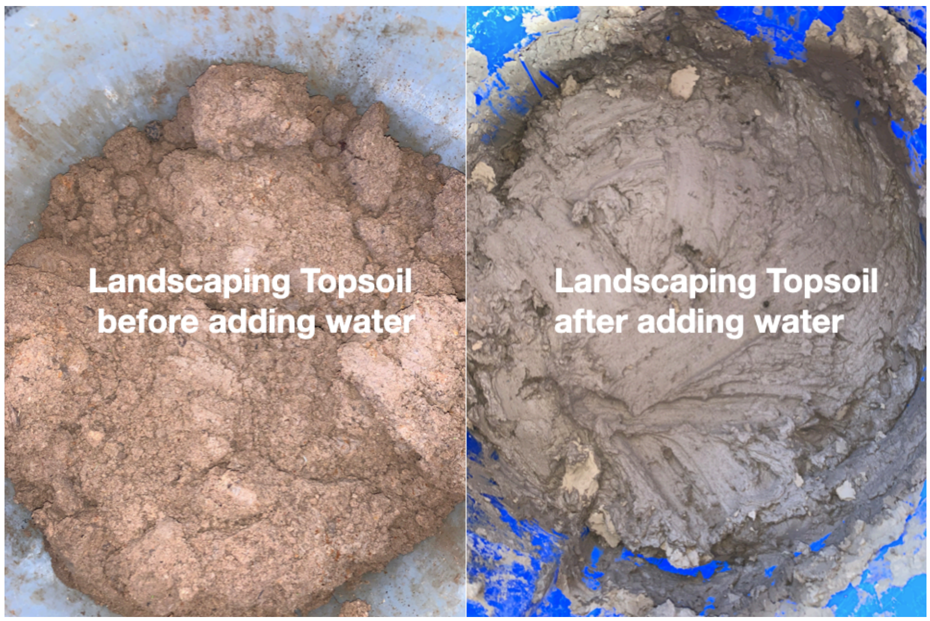

Figure 12: Landscaping topsoil used for experiments. On the left is our dirt before mixing it with water to turn it into the mud on the right.

To collect core samples, the drop test procedures from Section 2.3.1 were repeated using the the new dart design equipped with the 22 mm and 34 mm hollow inner diameter spikes. After each drop, the penetration depth and the soil collection height inside the core sampler was measured. The dart was then carefully removed from the test soil, the spike was removed from the shell, and the collected soil sample was pushed and scraped through the opposite end using a rod into a cup. Afterwards the soil sample was weighed on a scale.

Another experiment was performed to determine the range of water content the core sampling method of retrieving soil works with. Both hollow spikes were manually dipped into 2 kg of the mud mixture 0.5 m deep, pulled out, and held vertically for 30 seconds to inspect for mud slippage. Then 20 g of water was stirred into the mixture, and the procedure was repeated until mud slipped out of the hollow spikes.

3.2.2 Soil Collection

The amount of soil collected by the 22 mm and 34 mm hollow darts after they were dropped from 1 m and 2 m is plotted in Figure 13a. This plot shows an expected trend between core diameter and amount of soil collected; the larger diameter collects more soil. However, soil collecting behavior is not as easily predictable when considering the height of the column of soil inside the hollow spike. This height (the distance of mud inside the hollow spikes) is plotted in Figure 13b for both spikes dropped from 1 m and 2 m. The penetration depth into the soil after drops from 1 m and 2 m of both diameter hollow spikes are compared in Figure 14a, and the penetration depth of a hollow spike is compared to that of a solid spike (both with 40 mm outer diameter) is compared in Figure 14b. The hollow spike penetrates deeper than a solid spike when dropped from the same height.

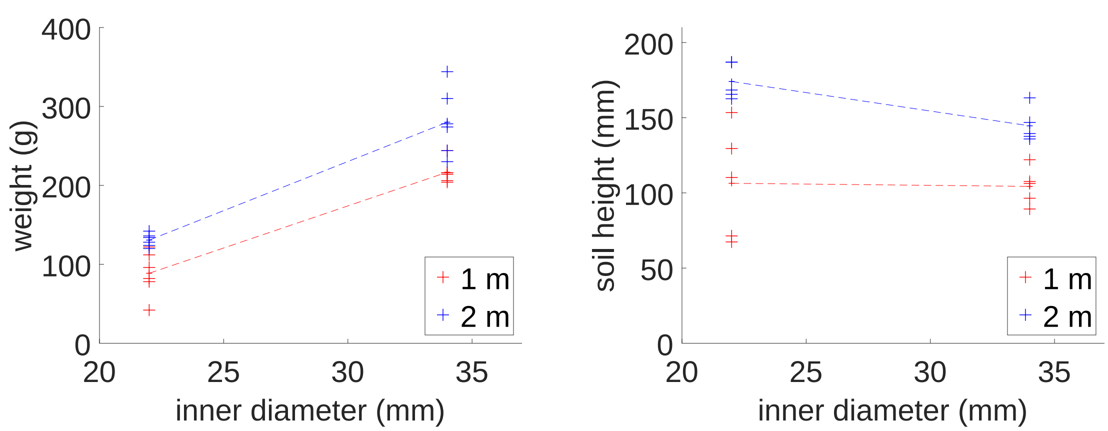

(a) soil collected (b) soil height

Figure 13: (a) shows the weight of soil collected for two dart inner diameters dropped at two heights with hollow darts. (b) shows the height of the soil collected inside the sampler for two diameters at two drop heights with hollow darts.

Comparing Figure 13a with 14a shows that even though a smaller diameter core sampler penetrates deeper into the soil, the larger diameter core sampler collects more soil. However, the moisture content experiment described in 3.2.1 gives further insight on how the soil resistance behaves at different moisture contents with the two different diameter hollow spikes. In this experiment mud started to slip out of the 34 mm inner diameter spike at 42% water content, while mud stayed inside the 22 mm inner diameter spike until a water content of 50%. Section 3.3 presents a sampling technique that also works with water content greater than 50%.

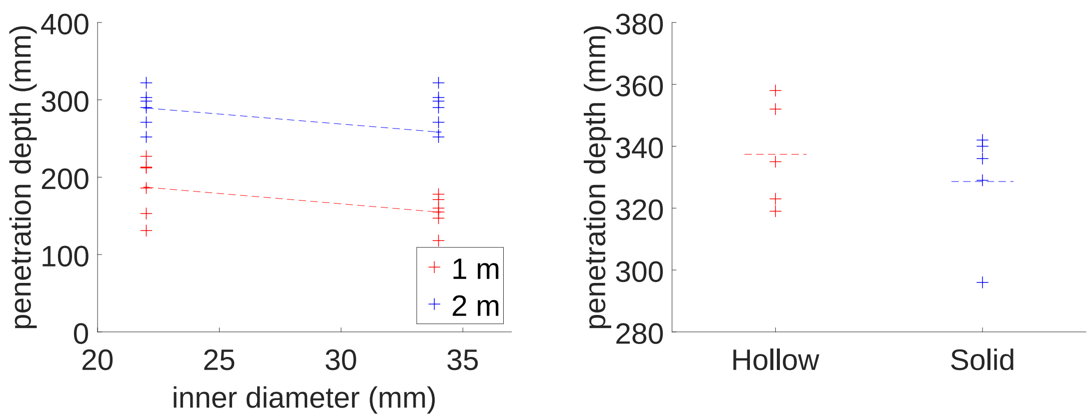

(a) penetration depth

(b) penetration depth at 3m

Figure 14: (a) shows the penetration depth of the dart for two inner diameters dropped at two heights. (b) compares the penetration depths of a hollow and solid spike dropped from 3 m (both have a 40 mm outer diameter.)

3.2.3 Effects of Core-Sampling on Deceleration

For each of the drop test experiments, the instrumented dart was raised to a drop height and released into a 180 L recycling bin using a pulley suspended by a rope just as in 2.3.1. The drop heights were measured from the tip of the dart to the surface of the soil in the recycling bin. The drop heights tested in these experiments were 1 m, 2 m, and 3 m. Refer back to Figure 6 for an example of a drop test from 3 m.

Figure 15 shows plots that compare the impact deceleration profiles of hollow and solid spikes dropped from the three heights. The hollow spike used here had an inner diameter of 34 mm and both spikes had an outer diameter of 40 mm. As expected, solid spikes experience greater deceleration peaks than hollow spikes. This behavior is most evident in Figures 15a and 15c when the darts were deployed from 1 m and 3 m. Whenever the darts are deployed from 2 m, as plotted in Figure 15b, the difference was not easy to detect.

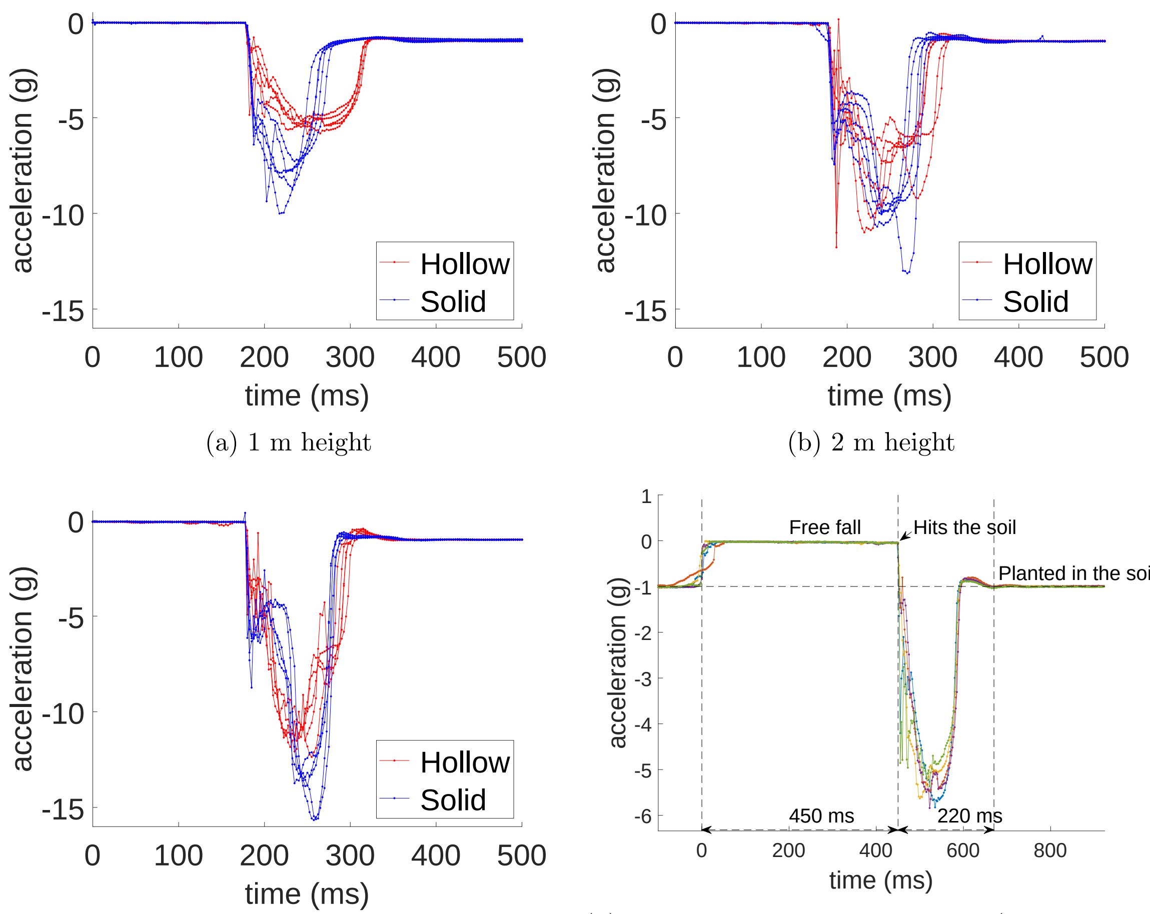

(a) 1 m height

(b) 2 m height

(c) 3 m height

(d) Labeled representative timeline (using the hollow 22mm diameter spike, dropped from 1m)

Figure 15: Impact deceleration plots of the 40 mm outer diameter tips (solid, and 34 mm inner diameter hollow) from three different drop heights into soil. 15d shows a representative timeline of deployment and impact.

At all drop heights, it appears that the hollow spikes (shown in red) take longer to decelerate, which would produce a difference in the displacement and velocity profiles after integrating this data. The displacement and velocity profiles obtained by integrating and double integrating the deceleration from Figure 18 is shown in Figure 16. The penetration depth that was manually measured for five dart drops for a 22 mm inner diameter hollow dart is around 200 mm (see Figure 14a). This is approximately the displacement seen in Figure 16.

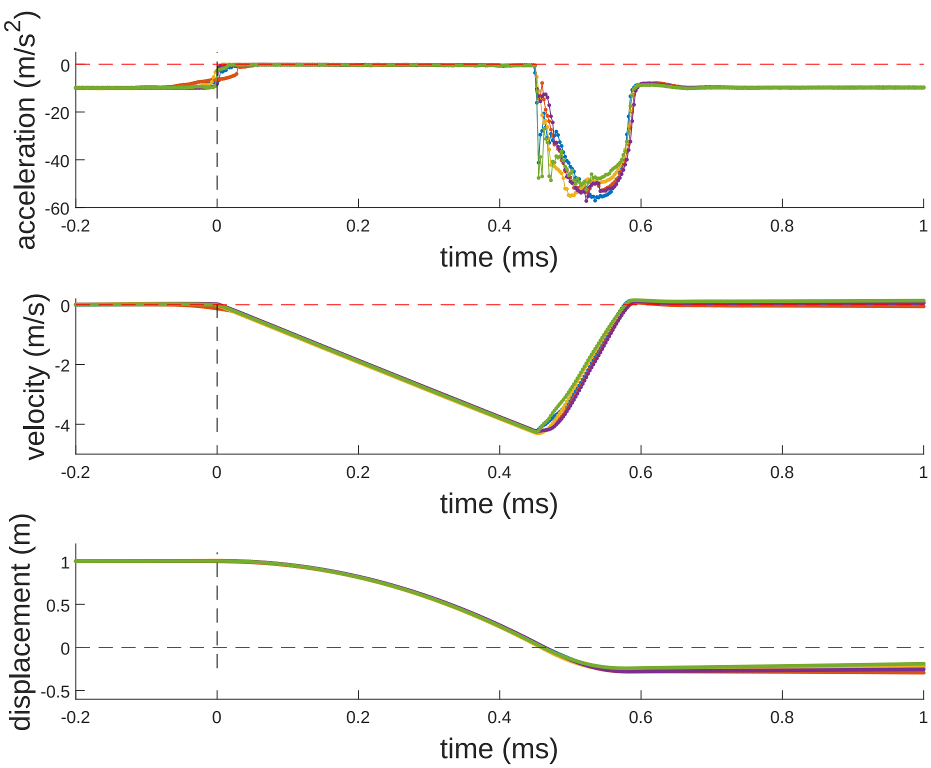

Figure 16: Velocity and displacement profile obtained by integrating the acceleration data from a drop test.

A closer look at the deceleration profiles of the same dart dropped from three heights is plotted in Figure 17; Figure 17a shows the hollow spike profiles and Figure 17b shows the solid spike profiles. These profiles plotted together show that not only do the solid spikes experience greater deceleration peaks, but they are also easier to distinguish. The hollow spike deceleration profiles are harder to distinguish at different drop heights, which might make distinguishing different soil types as in Section 2.3 more challenging, though this was not attempted in [2].

The deceleration profiles comparing different diameter hollow tubes are shown in Figures 18a and 18b. It is clear from these plots that the difference in diameter of the hollow tubes shows a greater difference in the deceleration profiles when dropped from lower heights.

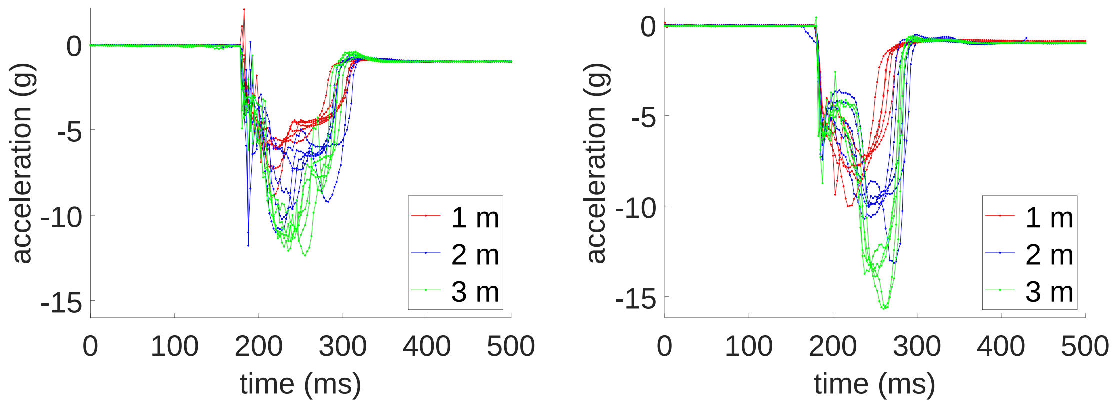

(a) Hollow (b) Solid

Figure 17: Both of these dart spikes had an outer diameter of 40 mm.

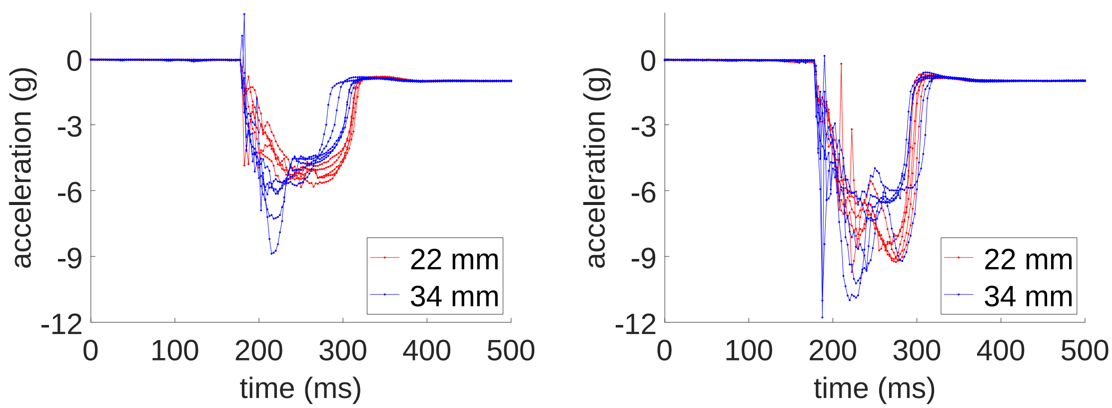

(a) 1 m height (b) 2 m height

Figure 18: Plot of the impact deceleration of the hollow dart tip for from two drop heights into soil with different dart diameters.

3.3 Collecting Soil Samples at Multiple Locations

The core-sampling dart tip presented in Sec. 3.1 can only sample at one location. This section presents an alternate dart tip design that enables our FFP to take depth-registered soil samples at multiple locations using the same tip. Though each of these samples are only 0.8 mL, this amount of soil is suitable for supporting microbiological and geochemical characterization. The procedure is illustrated in Fig. 19.

The dart consists of an outer sheath and an inner rotating sampler. The sampler is actuated by an internal servo motor (Fig. 19a). The sheath has a single vertical column of eight sampling holes. These holes are beveled to slice through the soil in a design inspired by a medical biopsy robot [39]. The inner rotating sampler has four columns of sampling pockets that match the outer holes. Each pocket can hold 0.8 mL of soil. By rotating the inner sampler, different columns can be exposed to the outer soil. The dart is dropped with the pockets sealed. In our demonstration, we manually drove the the dart tip into a jar of wet soil (Fig. 19 c). Once in the soil, the inner sheath is rotated to expose a column of pockets to the soil. After the sampler is in the soil, lateral earth pressure pushes samples into the pockets. After a predetermined wait time, the inner sampler rotates to seal off the pockets and the dart is ready for retrieval. In the future, this wait time could be defined by the soil type, where the soil type is determined by the deceleration profile.

For the demonstration illustrated in Fig. 19, a 0.2 kg-m servo motor (HiWonder LD-20mg) was connected to a wireless receiver (X8R) and controlled with a wireless transmitter (FrskyX9D).

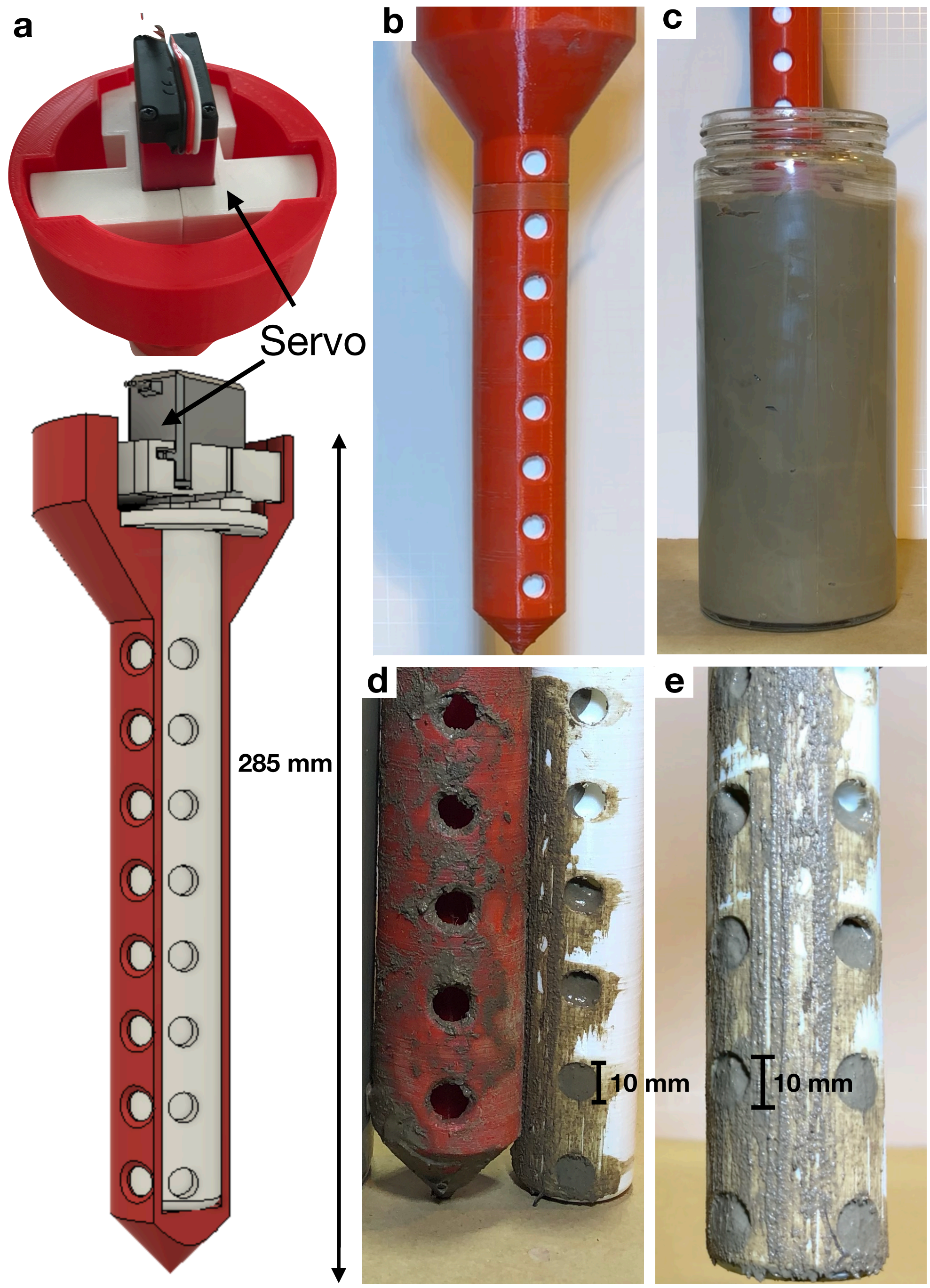

Figure 19: Soil collection system. The rotating sampler is inside a sheath. Rotating the sampler reveals pockets that allow sampling mud at different depths.

4 Retrieval

This chapter focuses on retrieving the dart developed in the previous two chapters. Section 4.1 presents a mechanism from [2] design that enables deploying and reeling in the FFP dart for multiple soil strength tests from a drone. Selected experiments from [1] show the forces required to pull a planted dart from wet soil and the pull force limitations of a drone. A solution for eliminating the extra force when pulling a dart from wet soil is also presented.

4.1 Retrieval Mechanism

A retrieval mechanism was designed around a fishing reel so that a drone could retrieve and redeploy the same dart for multiple penetration tests. A drone-mounted fishing reel can reel in a tethered dart on a spool, while the friction-less release enables the dart to fall freely during deployment. The reel (Abu Garcia Baitcast Silver Max 2) is housed between two plates. A 0.2 kg-m servo (HiWonder LD-20mg) is used to press the release button, and a 12 V DC motor (131:1 Polulu Metal Gearmotor 37Dx73L) is used to wind the reel. The DC motor is attached to the handle of the reel through a gear train. This DC motor is driven by an L298N motor driver and powered using a 12 V LiPo battery. For the demonstrations submitted with [2], both motors were controlled using a wireless transmitter/receiver (Frsky X9D). The mechanism is shown in Figure 20.

4.2 Forces Required to Pull a Planted Dart From Soil

The force required to extract a dropped dart varies with the pulling angle and the speed of pulling. To measure the pull force required to remove a planted dart from wet soil, the FFP was buried into wet soil and the force was logged while pulling it out. The FFP used for these experiments was the one developed in [1]. The dart was planted so that the entire length of the spike was buried (340 mm) into a 37 L recycling bin that was filled with the saturated mud from Section 2.3.1. To pull the the dart out, a stepper motor actuated a one meter long linear stage (OpenBuildsPartStore.com C-Beam). The linear stage pulled a

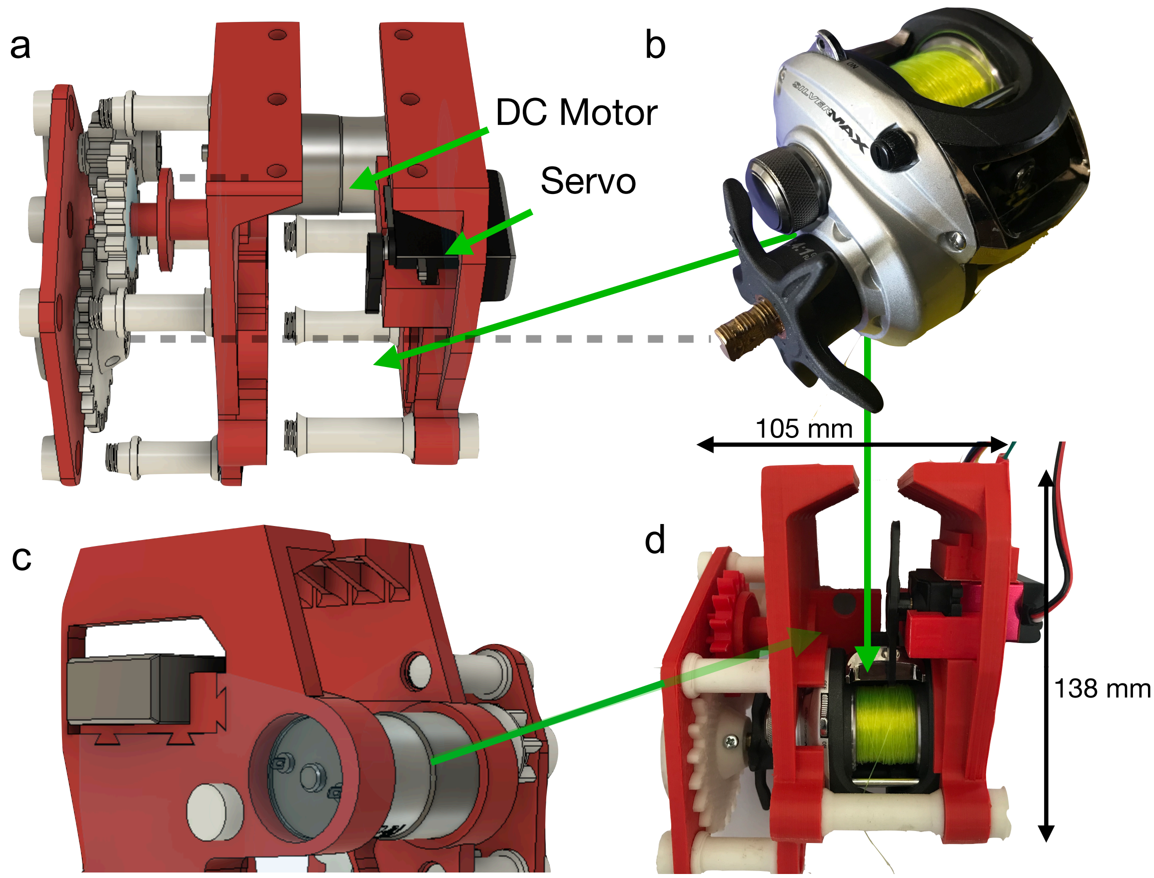

Figure 20: (a) Exploded view rendering of our retrieval mechanism, (b) fishing reel, (c) orthographic view, (d) actual assembled system.

1.5 mm steel cable, attached to an s-type load cell (10 kg CALT) that was fixed to the tail end of the dart. For all tests involving the load cell, the force was measured and logged by interfacing a load cell amplifier (HX711) with a serial synchronous interface. For each pull test, the soil was tamped flat before burying the dart. Figure 21 shows the setup: the linear rail, the load cell, and the dart.

For the fastest velocity tested, (333 mm/s), a power drill was used to rotate the threaded rod on the linear actuator. For the slower pull velocities, 27.3 mm/s and 13.6 mm/s, the threaded rod was rotated using a stepper motor. To vary the angle that we pulled the dart out of our mud, the pulley remained stationary, and the container of soil with the buried dart was moved horizontally, taking care to ensure the dart remained vertical. The pull angle was defined as the angle from horizontal of the cord that pulled the dart.

In Figure 22, the pull-out force was measured as a function of velocity at a constant angle

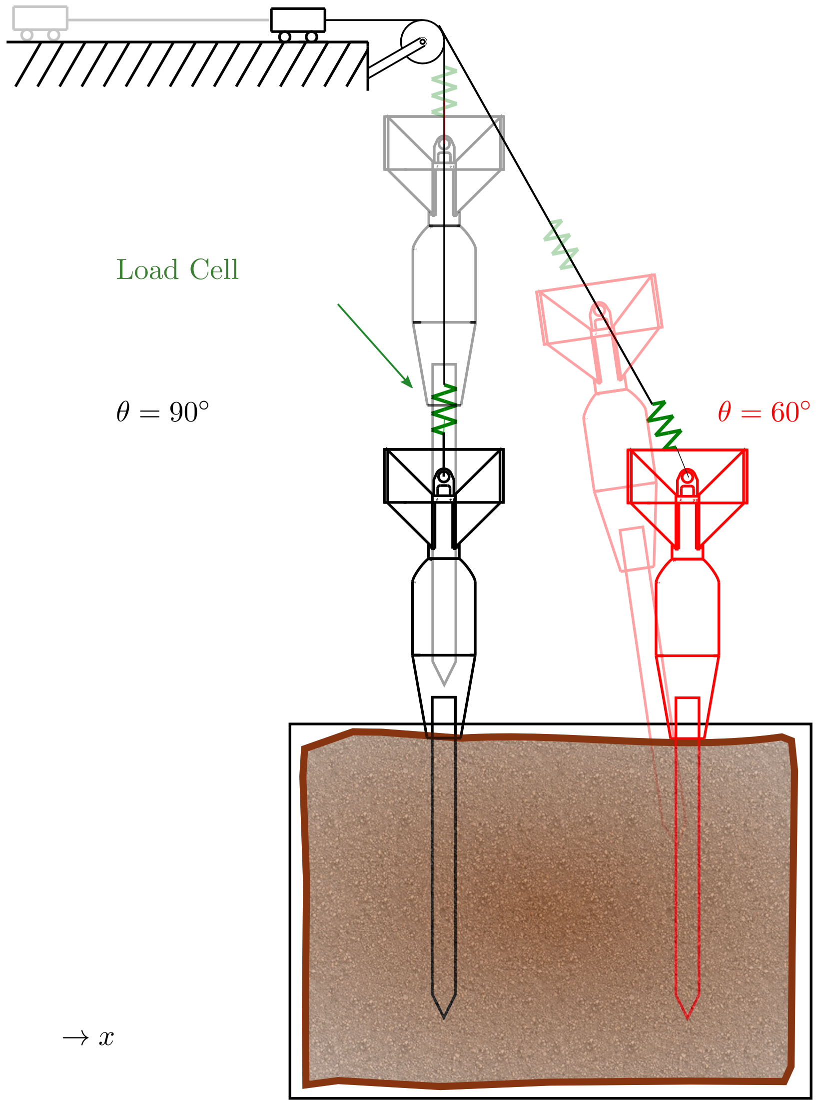

Figure 21: Experimental setup for measuring the force required to pull a dart from soil. To make different pulling angles θ, the container of soil is shifted along the x-axis. Shown are $\theta = 90^\circ$ and $\theta = 60^\circ$.

of 90°. As the speed increases, the pull-out force also increases. For example, a pull-out force of approximately 2 kg is necessary at 13.6 mm/s, 3.5 kg for 27.3 mm/s, and 4 kg at 333 mm/s. The increase in pull force is attributed to the viscoelastic behavior of soils, where increasing strain rate increases the strength of the soil. As a result, the increasing speeds correspond to increased strain rates and the pull-out force is concomitantly increasing.

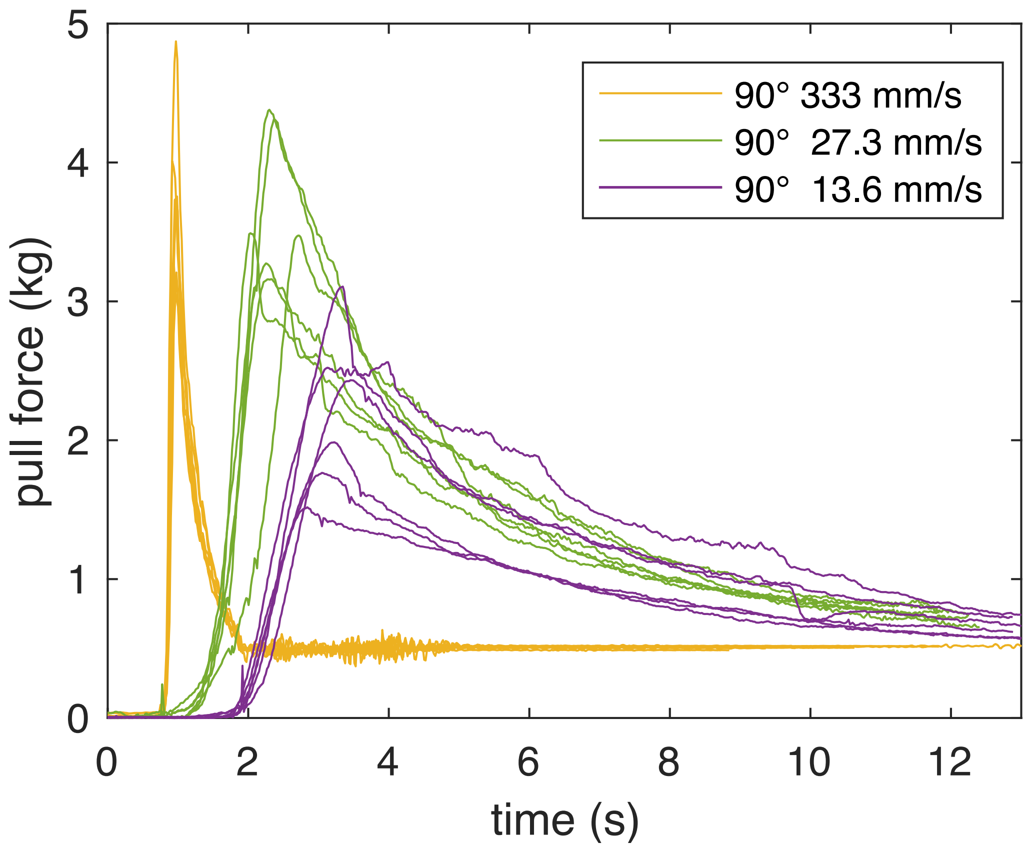

Figure 22: Pulling darts from saturated mud at different speeds. Faster speeds increase the maximum pull force.

Figure 23 shows the force required for pulling the dart out from different angles. The tests were completed at three different angles of 70°, 80°, and 90°. The highest pull force of 3.5 kg corresponds to 90°, while 70° pull force is lower at approximately 2 kg. In other words, the required pull-out force is higher by a factor of 1.75 with 90° compared to 70°. The reason for this behavior is twofold. The 90° test is located directly under the pulley while the 70° shifts to the right. A moment is exerted when pulling commences. Also, the rotation of the dart at 70° breaks the adhesion of the mud to the dart. This makes it easier to pull the dart out. The lateral restraint (bearing capacity) of the mud is also less than vertical suction as the dart rotates.

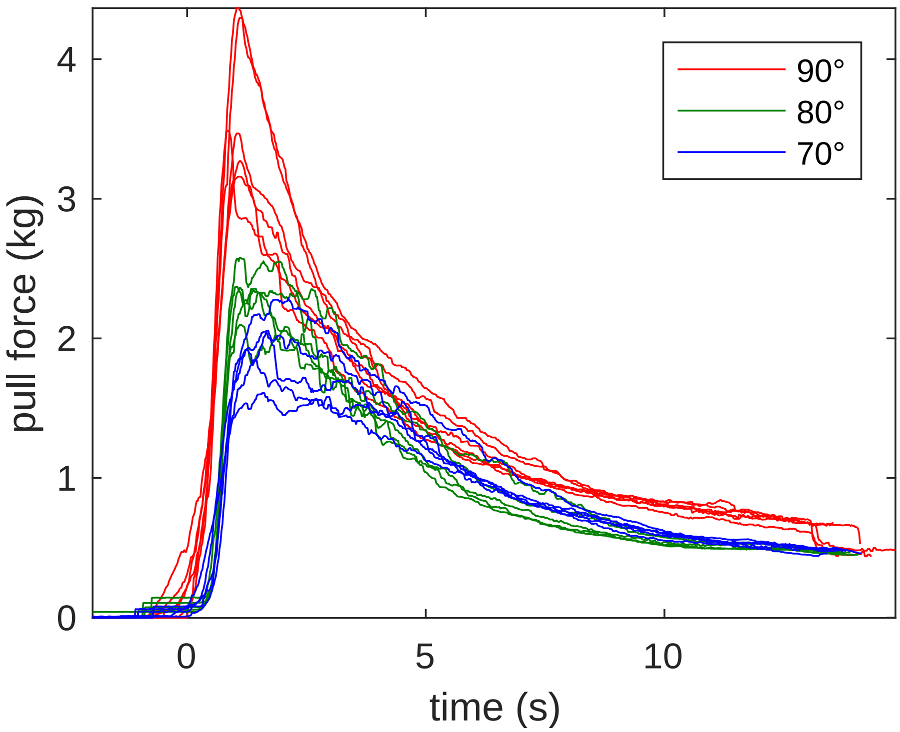

Figure 23: Pulling darts from saturated mud at different angles from vertical. See Fig. 21 for definition of pull angle. All pulls were at 27.3 mm/s using a linear actuator, and the darts were buried 340 mm in the soil.

4.3 Limitations of Pulling With a Drone

The setup shown in Fig. 24 was designed to measure the pull force exerted by a drone. It contains a s-type load cell (10 kg, CALT) attached to a bearing block constrained to rotate about one axis. The load cell is counterweighted on the other side of the bearing block. While the base is held static, the tension on a cable attached to the bearing block through the load cell can be measured while a drone pulls on it. To measure the drone pull force at different angles, the drone can fly diagonally upwards and the direction can be measured as an angle from horizontal using a protractor on the side of the base. The drone used for these pull tests was a DJI Mavic Pro 2 with a rated take-off weight of 907 g.

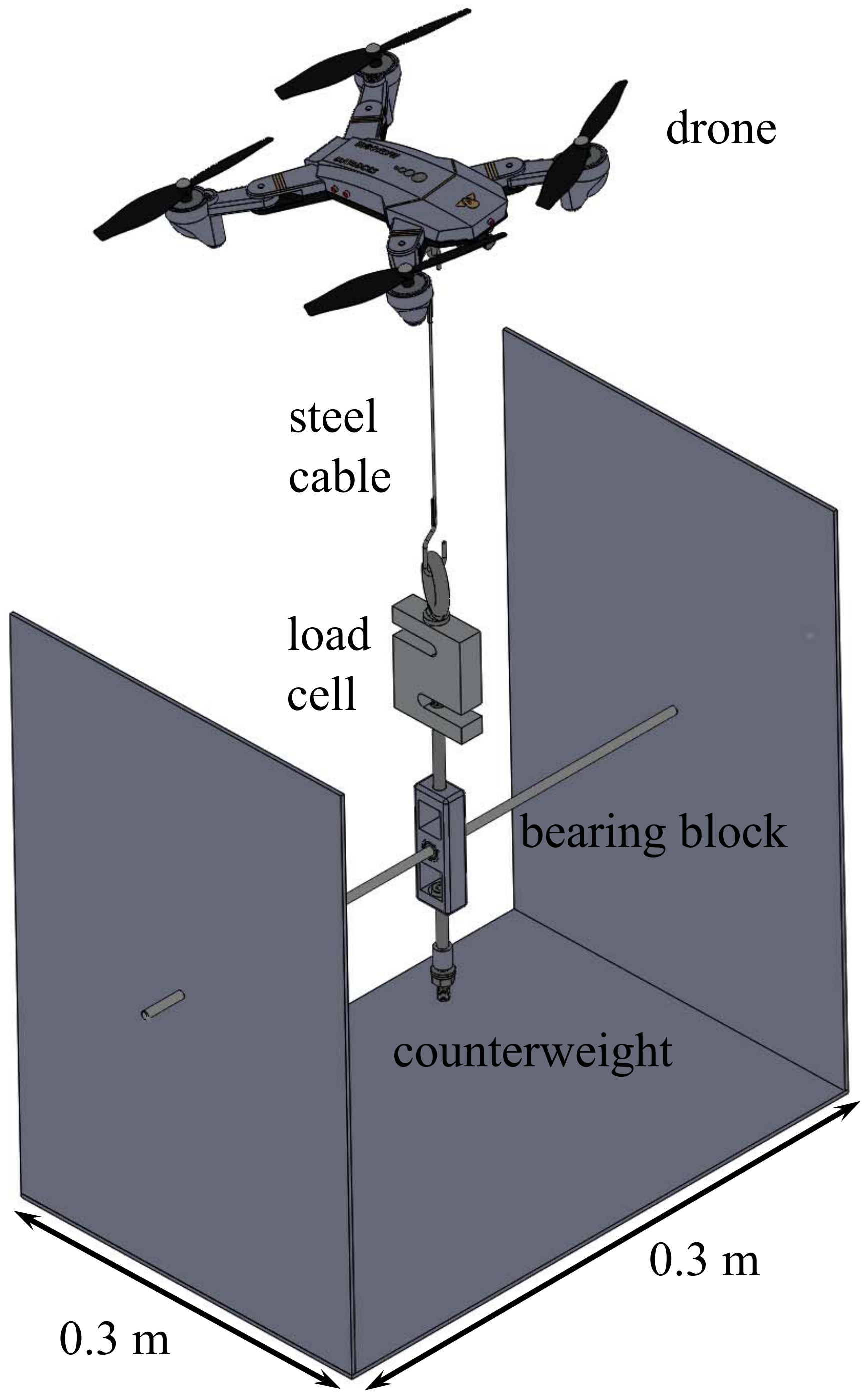

Figure 24: Testing setup for measuring the pull force of a drone.

The results for the drone pull tests are plotted in Figures 25 and 26. Figure 25 shows the forces exerted by a drone pulling straight upwards at maximum thrust to exert an impulse on the cable. In each of the three trials, the forces exhibit an oscillatory transient that dies out after approximately 1 second. This transient behavior consists of a range of values that peak at 2.4 kg. The steady state force is uniform, stabilizing to 0.82 ± 0.02 kg. This indicates that the maximum lift force available from this drone is insufficient compared to the required pull force in Figures 22 and 23. The steady state pull force of the drone for ten trials at four different angles is plotted in Figure 26. The force at 60° is 0.52 ± 0.18 kg, at 70° is 0.70 ± 0.06 kg, at 80° is 0.81 ± 0.03 kg, and at 90° is 0.82 ± 0.02 kg. For both of these tests, the drone was manually piloted.

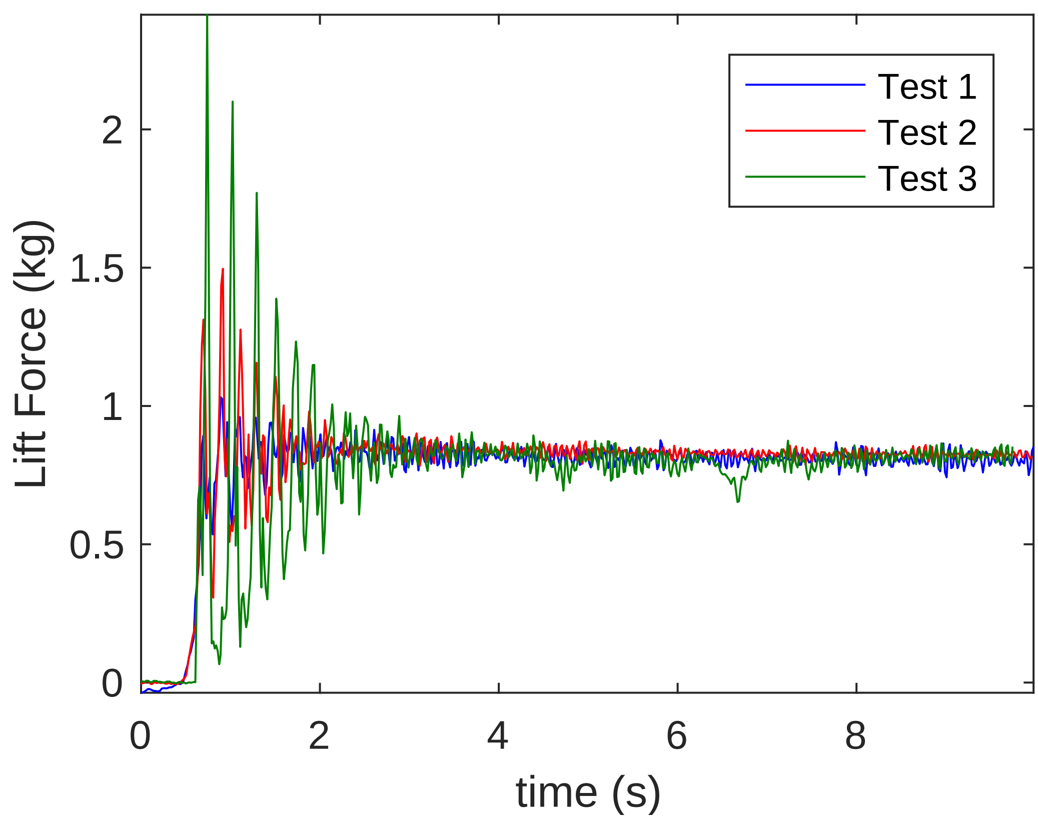

Figure 25: Maximum drone lift at 90° during three trials pulling on a load cell using the testing rig shown in Fig. 24. After a 1 second transient, with force ranging up to 2.4 kg, the force stabilizes at 0.82 ± 0.02 kg.

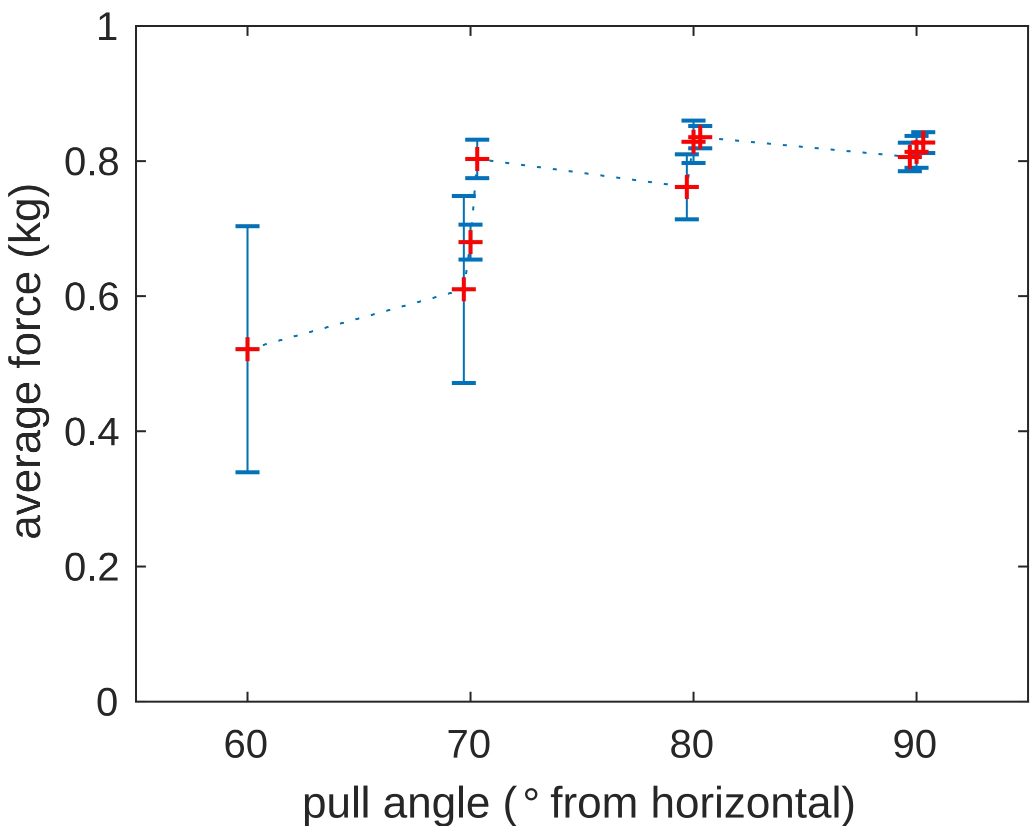

Figure 26: The drone steady-state pull force is maximum at 90°, and has the least variation. Each error-bar shows the mean and standard deviation for a test for 7 seconds of steady-state pulling at the desired angle.

4.4 Sacrificial Sleeve

One way to overcome the soil resistance when pulling a planted dart from soil is to deploy the dart with a sleeve around the spike. This sleeve is to be left behind when retrieving the dart, which reduces the force required for retrieval because the dart spike no longer has contact with the soil. Figure 27 shows an illustration of retrieval with and without a sacrificial sleeve.

For a demonstration, a sacrificial sleeve was made of PLA and designed to fit the spike of the dart. The sleeve had a wall thickness of 2 mm, and used a thin foam gasket between the top of the spike and the dart body to prevent the sleeve from jamming onto the spike. Future implementations could use a servo to release the sleeve, but in this demonstration, a thin strip of duct tape was used to secure the sleeve to the dart during the deployment,

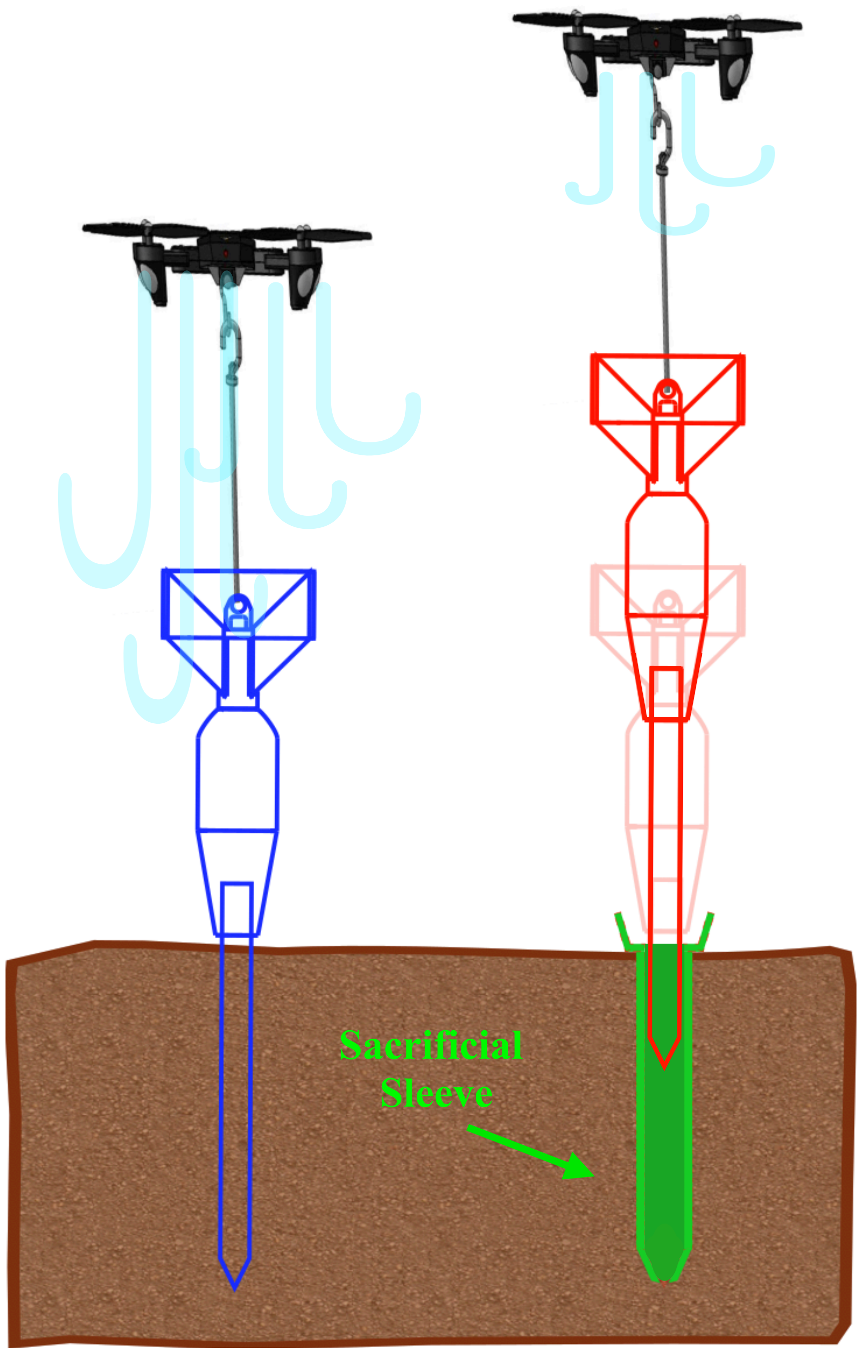

Figure 27: Technique for retrieval of a drone-deployed FFP using a sleeve that is left behind. See Figure 28 for a plot of the pull force with and without this sleeve.

and manually removed before retrieval. After the drone dropped the dart into the saturated mud used in Section 2.3.1, a load cell was attached between the drone and the dart, and the pulling forces were recorded. This experiment shows the difference in pulling force required to retrieve a bare dart with the pulling force required to remove a dart whose spike was in a sacrificial sleeve that was left behind. Figure 28 shows the forces exerted as the drone attempted to retrieve the dart with and without a sacrificial sleeve. Using a 3D-printed sacrificial sleeve on the dart enabled successful retrieval.

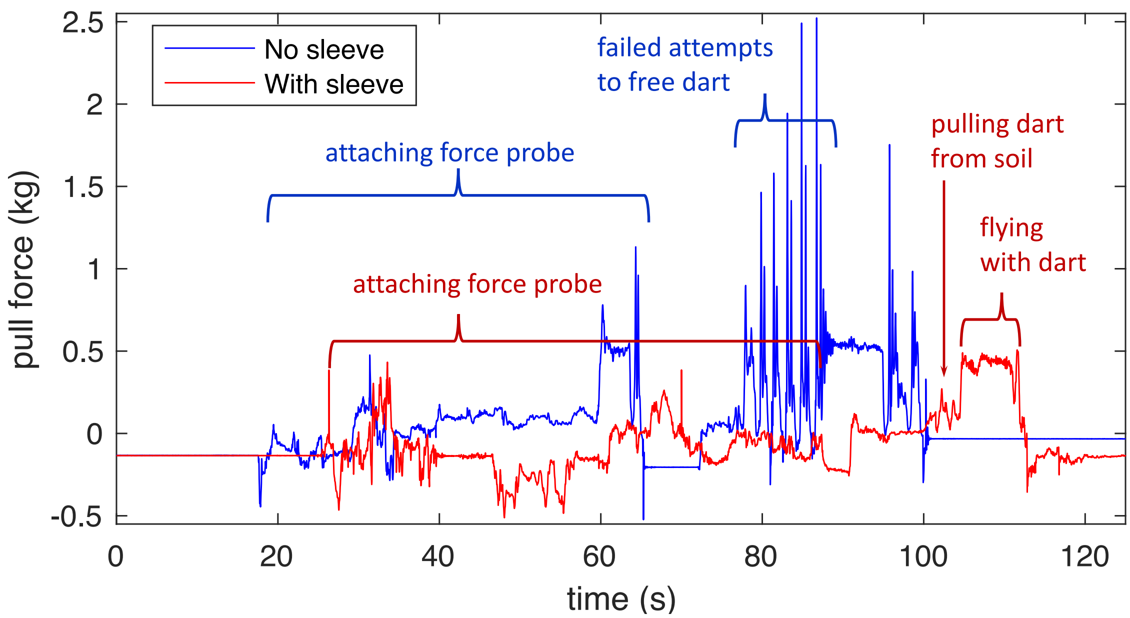

Figure 28: After the drone dropped the FFP, a force probe was mounted between the drone and the dart to measure pulling forces. Three trials were performed using the bare FPP and three trials where the FFP was covered with a sacrificial sleeve.

Figure 29: Six frames showing successful repeated deployment and retrieval of the FFP.

4.5 Conclusions On Retrieval

Though the only drone tested for the force pull experiments was a DJI Mavic Pro 2, it appears that a drone can exert an impulse on planted dart with a greater peak force than its rated take-off limit. In the case of the experiments in Section 4.3, the force was two times greater than the rated take-off limit. Using this drone to pull the dart when buried 340 mm into soil with a moisture content of 30.5%, retrieval is still not possible. In practice, a stronger drone must be used. Experiments also showed that pulling a dart from wet soil slowly and at an angle reduces the force required. But even though the dart is easier to pull out at an angle, the drone pull force reduces when pulling at an angle.

Deploying a FFP dart with a sacrificial sleeve is effective in eliminating the resistance forces imposed on the dart during retrieval. However, the sacrificial sleeve retrieval method requires modification to use the discrete-sampling spike tip design from Section 3.3. Collecting core samples, and performing repeated penetrometer tests using the same dart is still possible with a sleeve around the spike, given that the sleeve is replaced in between tests.

A final video demonstration was submitted with [2] that showed two successive deployments followed by two retrievals of a FFP dart during one flight, demonstrating the use of the retrieval mechanism. In this video, a licensed pilot flew a drone with the aid of two spotters and a fourth participant operated the deployment/retrieval mechanism using a wireless transmitter. A smaller and lighter version of the dart was used for this video; it did not contain the onboard electronics. The dart was also deployed into the mud created in Section 3.2.1 from a low height to reduce the penetration depth. The dart modifications and the deployment conditions were made to reduce the overall payload on the drone and to reduce the amount of pull force required from the drone during retrieval because the purpose of this demonstration was to show the effectiveness of the deployment/retrieval mechanism. Six frames from this video are shown in Figure 29, showing the flight, deployment, impact, reel winding, and UAV pulling steps.

5 Manipulation of Particle Ensembles

This chapter presents parts of work from [3] and [4]. These works study the manipulation of ensembles for the purpose of reconfiguration and localization. These methods of control are suited for problems where subjects are so small that they do not contain devices like sensors to determine their location or motors to control movement and actuation, so manipulation is achieved through outside global forces such as magnetic fields or gravity. In [3], particles use static boundary friction in triangles, convex polygons, and regular polygons for rearranging two particles, and static boundary friction in rectangular workspaces for the reconfiguration of multiple particles. [4] examines global input manipulation of particles inside planar geometries with curved boundaries. Tools that were designed to verify and demonstrate theories in [3] and [4] are presented here.

5.1 Related Work

Biomedical interests in ensemble manipulation include minimally invasive surgery, targeted drug delivery, and molecular self-assembly. [40] explores works where magnetic fields are used to actuate micro and nano robots in biological fluids, however communication between robots in liquid environments remains a challenging task that requires complex hardware [41]. The problem of controlling the respective positions of multiple small-scale robots can be approached by using the geometry of their environments. Work in [42, 43] shows that the individual positions of multiple objects under global input forces can be manipulated by designing obstacles into their workspace. The concept in these types of problems is that all objects move in one direction until they collide with an obstacle; then a sequence of directional movements can be designed to achieve the desired independent goal locations for the objects. Instead of using obstacles *inside* a workspace to relocate objects, the work in [3, 4] uses the *exterior* boundary geometry and friction with the exterior boundaries (workspace walls).

5.2 Using Boundary Friction for Particle Relocation

This section starts by examining a technique to re-position two particles in a triangular workspace. The only interaction with the particles is by tilting the workspace. Particles do not move for small angles of tilt, but once the workspace is tilted at an angle greater than the critical angle the particles slide freely until they hit a wall. Interestingly, the angle when a particle starts to slide can be different if a particle is resting against a wall.

A strategy for rearranging two particles in a triangular workspace using the friction at the floors and walls is developed in [3]. In this work, an angle of friction, θ is described as the angle that particles start to slide against contact surfaces when the surface is tilted, making the coefficient of friction between the two surfaces, $\mu := \tan\theta$. Referring to Figure 30, particles r_1 and r_2 can be given gravitational input fores, $u(t)$ by tilting the triangle around axes parallel to the walls. If $u(t)$ is beyond the cone of $\pm\theta$ from the normal of the boundary wall, N, the particles can overcome static friction at the boundaries and slide past them. If $u(t)$ is inside $\pm\theta$, they cannot move.

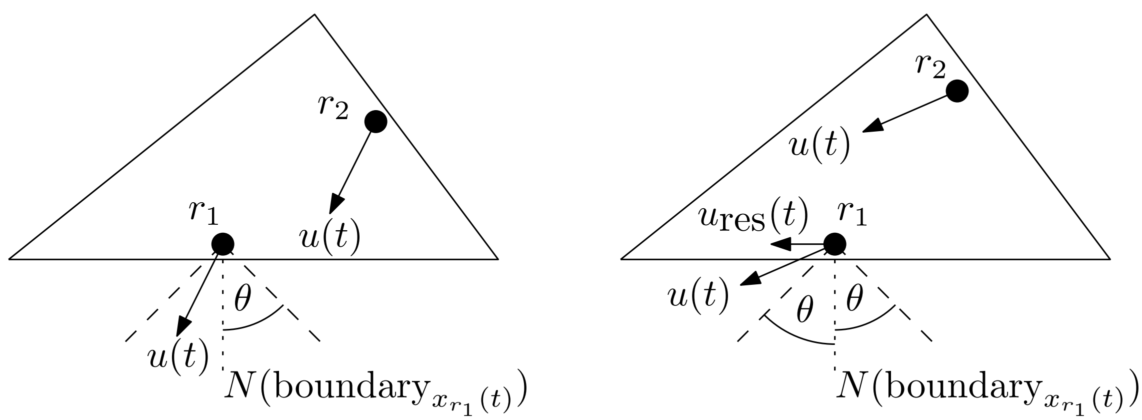

Figure 30: On the left, $u(t)$ is within $\pm\theta$, so only r_2 can move, but on the right, $u(t)$ is outside of $\pm\theta$, so both r_2 and r_1 can move.

5.2.1 Hardware Demonstration Setup

A setup to experimentally verify the theories on manipulating two particles inside a triangle using boundary friction in [3] is shown in Figure 31. A triangular workspace was made and held by the gripper of a UR-3 robotic arm to provide tilt inputs around three axes. The triangle was made from four pieces of laser-cut acrylic. The walls had the acrylic exposed, while the floor was covered in teflon oven liners. The red and blue particles were made of acrylic, and the bottom surfaces were covered with teflon tape. The wall's coefficient of static friction with the particle's contact surface (acrylic on acrylic) was approximately $\mu_w = 0.61$, and the floor's coefficient of static friction in contact with the particle (teflon tape on teflon oven liner) was approximately $\mu_f = 0.207$. These were measured by placing the particle on this surface and tilting until the particle first slides. The only force acting on the particles in these demonstrations was gravity.

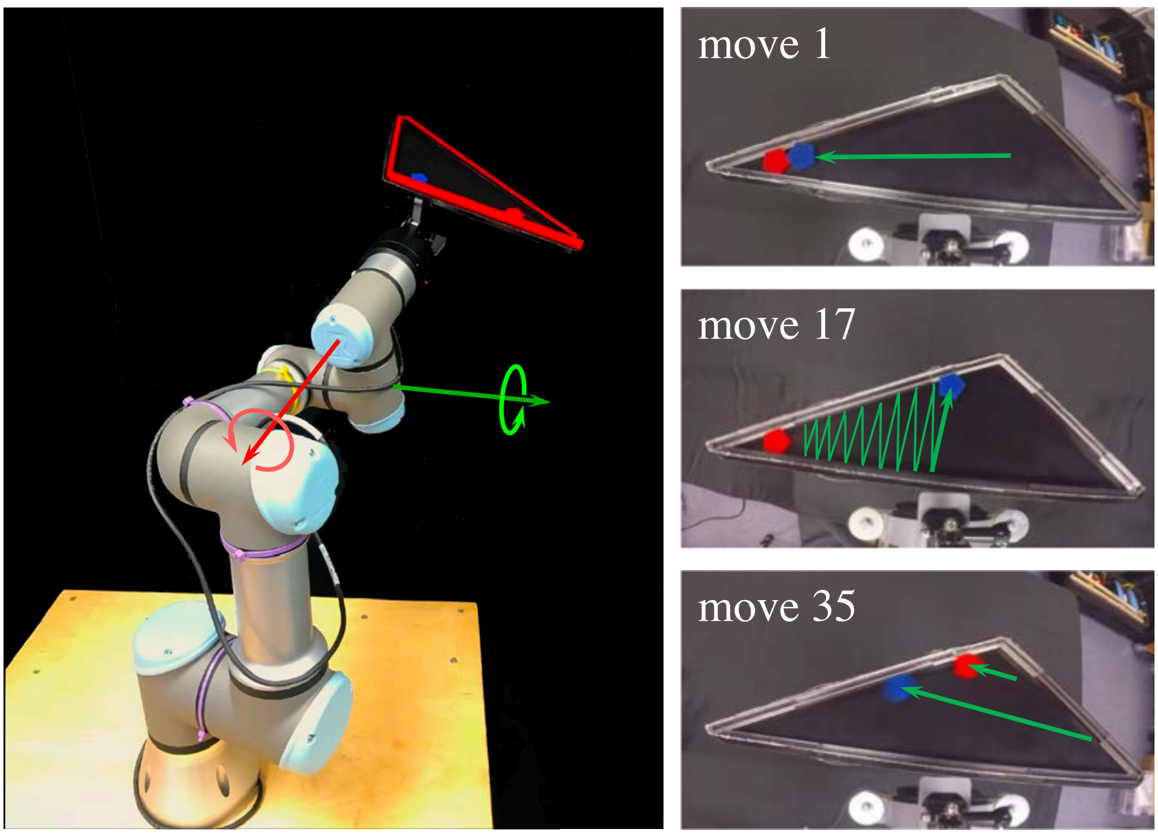

Figure 31: (Left) Using robotic apparatus to impose a global force on configuration of particles. (Right) A reconfiguration sequence that combines global force and local friction to achieve arbitrary repositioning of particles.

5.2.2 Model for Wall and Floor Friction

Referring to the diagram in Figure 32, any tilt of a 2D workspace can be described by first a tilt θ_w about the axis parallel to the boundary wall (such that positive θ_w slopes the workspace toward the wall), followed by a tilt θ_p about the axis perpendicular to the first tilt and the original gravity axis.

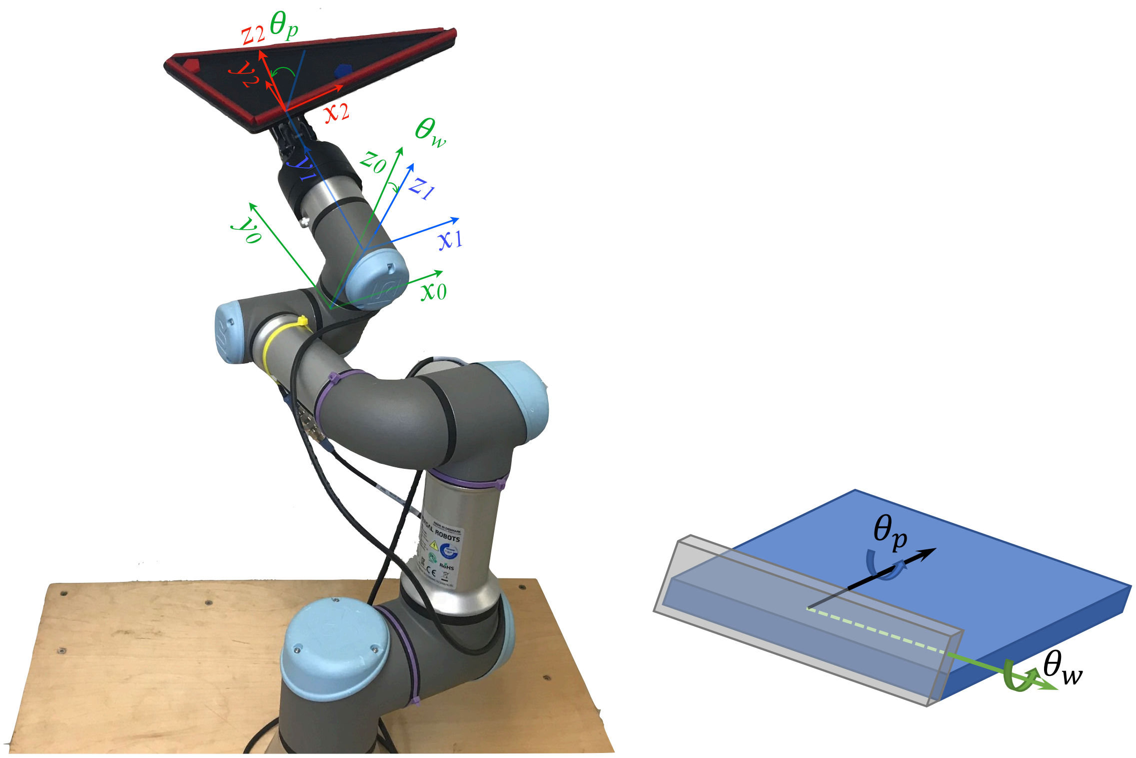

Figure 32: Triangular workspace on UR-3 used for model

A first rotation about the world gravity access can be applied (the z-axis) to align the boundary wall with the world x-axis, followed by a rotation θ_w about the current x-axis, and finally a rotation θ_p about the current y-axis to complete the composite tilt. The composite rotation can be described as

$$R_{z,\phi} R_{x,\theta_w} R_{y,\theta_p} = R_{z,\phi} \begin{bmatrix} c_{\theta_p} & 0 & s_{\theta_p} \\ s_{\theta_w} s_{\theta_p} & c_{\theta_w} & -c_{\theta_p} s_{\theta_w} \\ -c_{\theta_w} s_{\theta_p} & s_{\theta_w} & c_{\theta_w} c_{\theta_p} \end{bmatrix}. \tag{1}$$

In equation 1, the shorthand, $\sin(x) = s_x$ and $\cos(x) = c_x$ is used. For simplicity, the following analysis ignores the initial rotation about the z-axis. The third row describes how the components of the original gravity vector are distributed along the boundary wall ($-c_{\theta_w} s_{\theta_p}$), perpendicular to the wall (s_{θ_w}) and into the floor ($c_{\theta_w} c_{\theta_p}$). For simplicity, assume the force of gravity on the particle is 1N: $f_g = [0, 0, -1]^\top$. To contact the floor, both θ_w and θ_p must have magnitude less than $\pi/2$. The normal force from the tilted floor is $f_{\text{N,floor}} = c_{\theta_w} c_{\theta_p}$. If a particle is touching a wall *and* the tilt $\theta_w > 0$, then the wall generates a normal force,

$$f_{\text{N,wall}} = \begin{cases} s_{\theta_w}, & \theta_w > 0 \\ 0, & \text{else.} \end{cases} \tag{2}$$

The resulting force on the particle is

$$f_{\text{slide}} = f_g - f_{\text{N,floor}} - f_{\text{N,wall}}. \tag{3}$$

The static friction force is proportional to the normal force. The particle will only slide if f_{slide} is greater than the static friction force, i.e.,

$$|f_{\text{slide}}| > \mu_f |f_{\text{N,floor}}| + \mu_w |f_{\text{N,wall}}|. \tag{4}$$

The particle slides if the following quantity is positive:

$$\begin{cases} |c_{\theta_w} s_{\theta_p}| - \mu_f c_{\theta_w} c_{\theta_p} - \mu_w s_{\theta_w} & \theta_w > 0 \\ \sqrt{1 - c_{\theta_w}^2 c_{\theta_p}^2} - \mu_f c_{\theta_w} c_{\theta_p} & \text{else} \end{cases} . \tag{5}$$

The two-links of the robot arm generate a rotation about the global x-axis, followed by a rotation about the current y-axis: $R_{x,\theta_x} R_{y,\theta_y}$. To generate the appropriate gravitational force described by a z rotation of ϕ followed by θ_w about the wall and θ_p perpendicular to the wall, only the third column of (1) needs to be reproduced, and then select

$$\theta_y = \arcsin\left(c_\phi s_{\theta_p} + c_{\theta_p} s_{\theta_w} s_\phi\right) \tag{6}$$

$$\theta_x = \arcsin\left(\frac{s_{\theta_w} c_{\theta_p} c_\phi - s_{\theta_p} s_\phi}{c_{\theta_y}}\right). \tag{7}$$

5.2.3 Experimental Verifications

An experiment was performed to verify the slipping force model in (5). Figure 33 is a contour plot showing slipping force due to gravity minus static friction forces from the wall and floor. Regions with positive values will slip. Particles not at a wall will slip outside the green circle and particles at the wall will slip below the red line. On the right is a contour plot showing angle of friction.

$$\text{Angle of Friction} = \frac{\pi}{2} - \arctan(s_{\theta_p} c_{\theta_w}, s_{\theta_w}). \tag{8}$$

The 35 data points overlaid show where components slipped, as a function of tilt about the wall θ_w and perpendicular to the wall θ_p (see right image of Figure 32). The experiments moved both particles using the tilt marked by the blue point, and the purple point moved only the free particle.

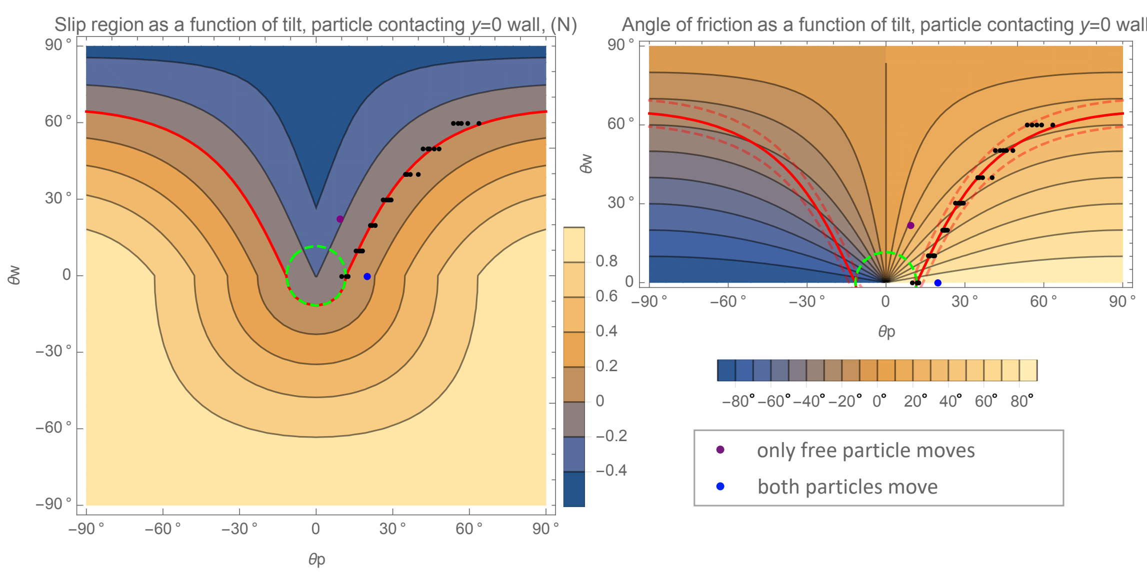

Figure 33: Contour plot showing the resulting force on the particle as a function of tilt.

A closer look at the tilt sequence used to switch the positions of a red and blue pentagonal particle is shown in Figure 34. The first frame shows the initial position of the two particles. In move 1, the triangular workspace is tilted so that the particles move to one corner together. Move 17 shows the blue particle moving along a zigzag path leaving the red behind due to the static friction of the walls at the corner. Moves 33-36 show how the switching of the particles takes place.

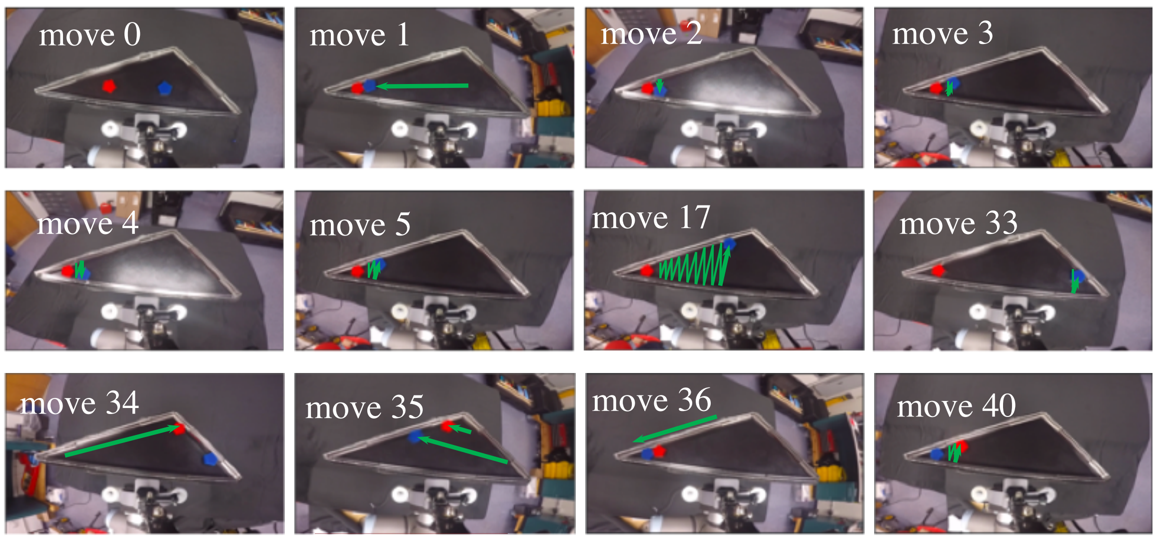

Figure 34: Two particles were placed into opposing corners of a triangle, and their positions are switched every 36 moves using procedures from Section III of [3].

Figure 35 shows a normal distribution fit to counts from 15 trials for two different boundary materials: acrylic and electrical tape over acrylic. When the particle impacts an acrylic boundary, it tends to slide along the edge, resulting in less required cycles than if the boundary is covered with electrical tape. This rejects the null hypothesis that the different surfaces require the same number of cycles with p-value 6.7×10^{-10}.

5.3 Moving the Boundary

The setup shown in Figure 36 was designed demonstrate motion models developed in [4]. Ensembles of objects are manipulated using the boundaries of their environment as in [3], except in [4], the boundaries are curved geometries and the models can account for slipping along the boundaries once they are reached. Details on these models including algorithms

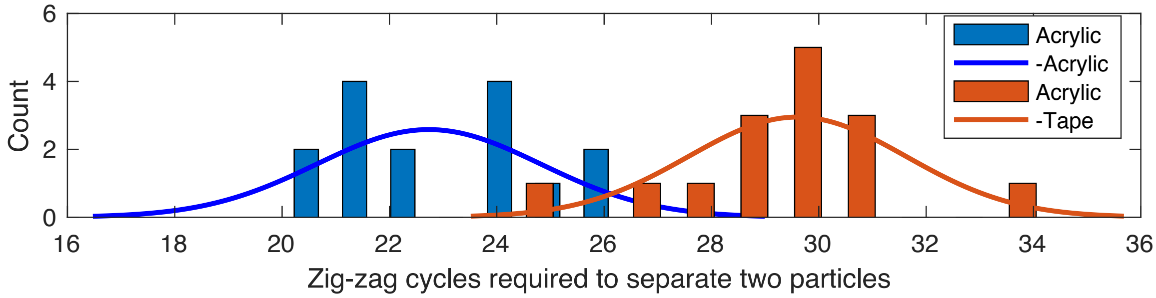

Figure 35: Histogram data on required number of zigzag movements required for two combinations of wall and particle materials.

for localization of ensembles within boundaries modeled as cubic Bézier curves can be found in [4], however this section only presents tools that were designed for physical proofs of these concepts.

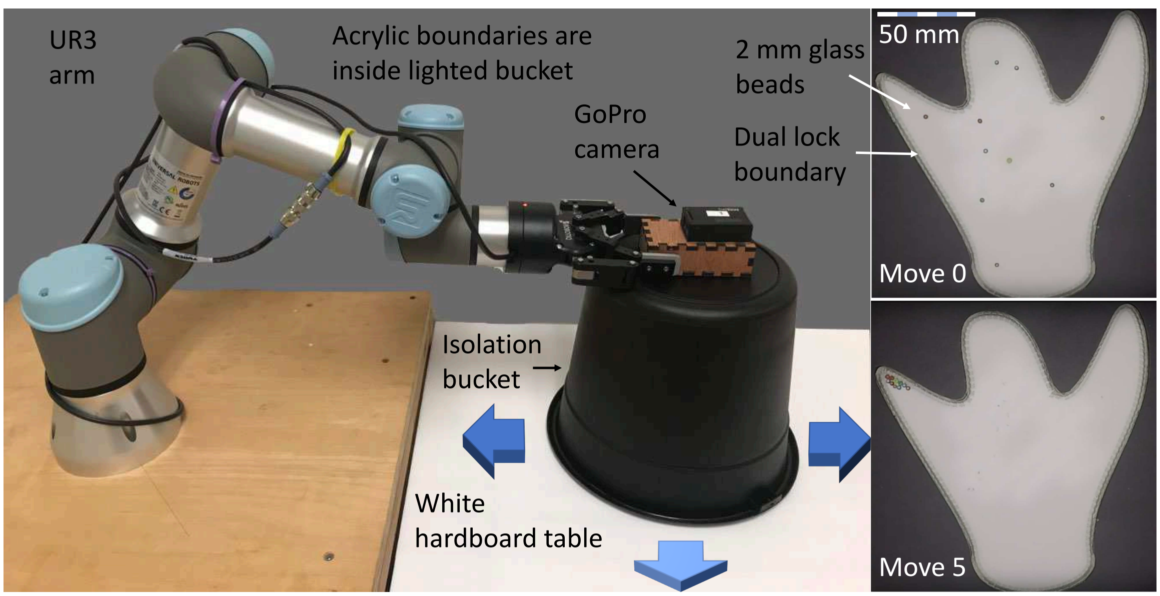

Figure 36: A sliding boundary setup designed to demonstrate motion models that aggregate objects by making use of their environment geometry.

The gripper of the UR3 in Figure 36 is holding a camera attached to an inverted plastic bucket looking down at objects within a curved boundary (on the right). The objects are 2 mm diameter glass seed beads. The curved boundary was laser cut from 6 mm acrylic and for a "sticky model" (one of the two models that assumed infinite friction in [4]) the curvature was lined with a thin strip of Dual Lock (3M Reclosable Fastener). The bucket and camera are then translated along the plane of the white hardboard table along a precomputed trajectory which aggregates the particles. Using this technique of moving the boundary instead of the objects simplifies experiments where the focus is on manipulation using boundary geometry and uniform input forces are assumed. Figure 37 shows eight frames of a sequence of five moves that aggregates 10 particles within a curved boundary using the setup presented.

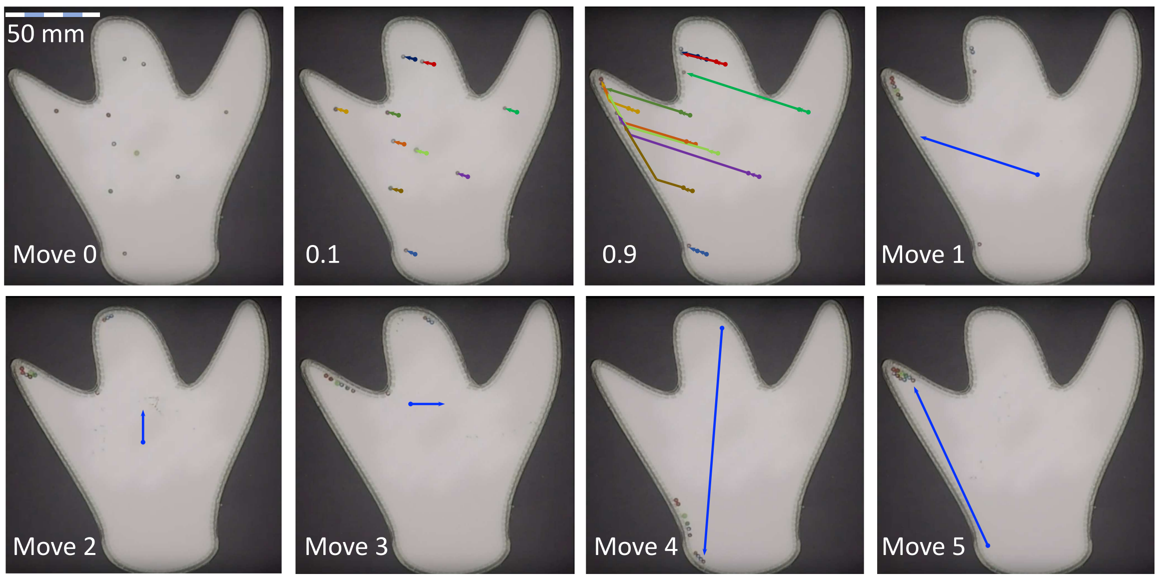

Figure 37: Aggregation of 10 particles within a curved environment.

The setup in Figure 36 was also used in [3] to demonstrate the rearrangement of three objects using boundary friction within a square. The sequence of moves accomplishing two different rearrangements of three objects is shown in 38. The blue moves show the reordering of objects three and two. That is, objects (1,3,2)→(1,2,3). The green moves show the reordering of all three objects. That is, objects (3,2,1)→(1,2,3). In the models developed in [3], all objects move when commanded unless friction with the boundary prevents motion. The objects here are 9 mm squares laser-cut out of acrylic, and the boundary is a 115 mm laser-cut square coated with 220 grit sandpaper.

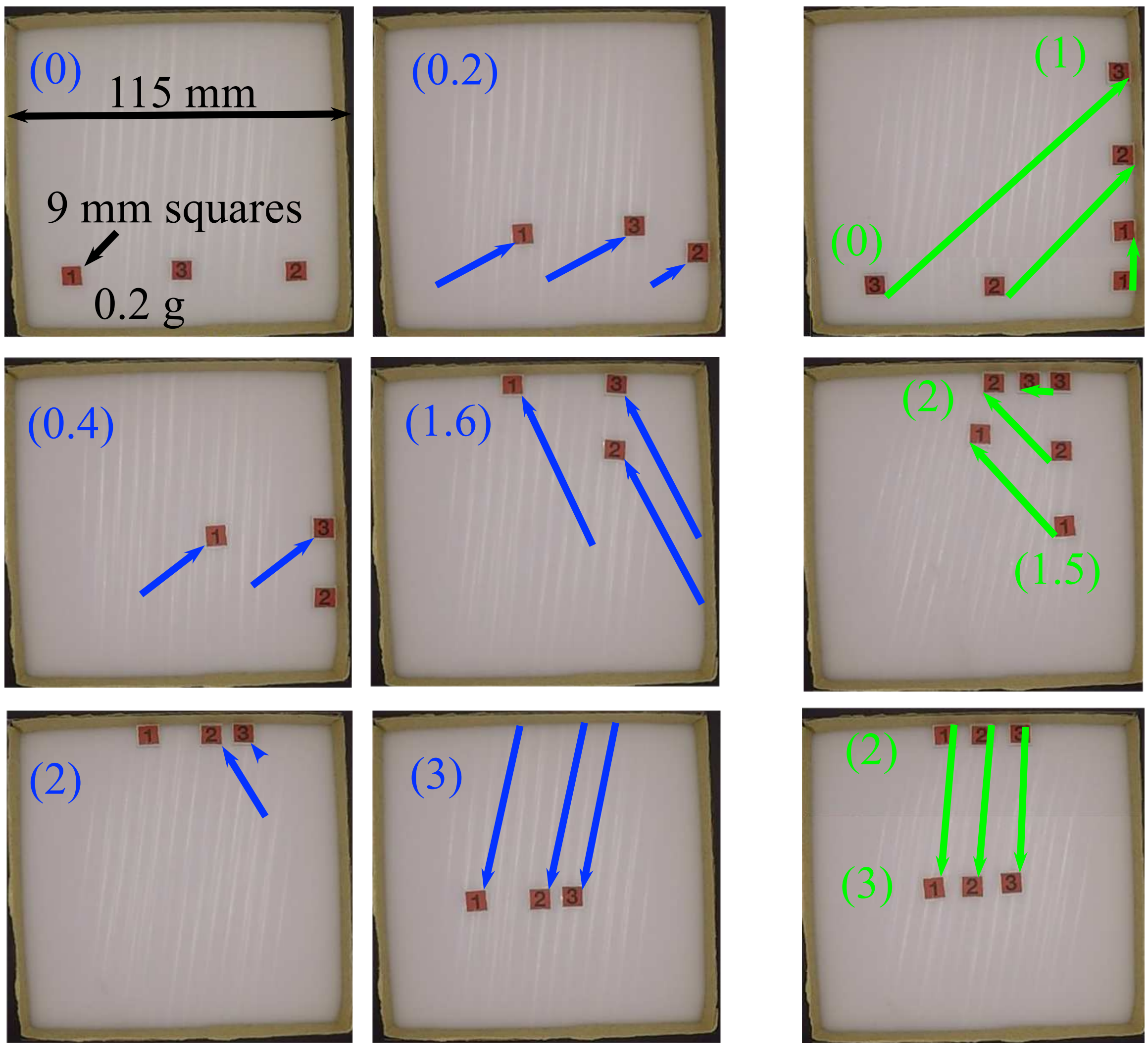

Figure 38: Reordering of three particles within a square using boundary friction.

6 Conclusion

The majority of this thesis introduced an instrumented dart designed to be deployed by UAVs into coastal wetland soils to retrieve soil samples while simultaneously performing soil strength measurements. Chapter 2 presented experiments that were performed with the dart that showed they could be used to distinguish three soil types. In these experiments, an onboard accelerometer measured in the deceleration upon impacting soils after being dropped from three different heights. Results implied the dart was effective in sensing the structural parameters of moist soils. Chapter 3 presented two different designs for the spike of the dart that were made to retrieve soil samples while simultaneously performing penetrometer tests. Tests using the modified dart spikes show the amount of soil that they collect, and also how collecting samples affects the penetrometer data. Results showed that the effects of collecting soil samples on deceleration cannot be neglected when interpreting strength measurements. Chapter 4 introduces the design of a mechanism that is capable of retrieving a planted dart redeploying it for repeated testing. Chapter 4 also provides insight into the effort that will be required when retrieving the dart from moist soils by measuring the pull force needed to pull a dart from soil, and also the pull force available from a small drone. Results showed that some techniques can be employed to reduce the force required to retrieve a planted dart, such as pulling slowly and at an angle. These extra forces due to the resistance on the dart exerted by the soil can be eliminated almost entirely, but the solution comes at the cost of not being able to use the more advanced, soil sampling spikes—at least for now. Chapter 5 switches the focus of this thesis and presents work on the manipulation of multiple small objects using the boundaries of their workspace. Hardware experiments prove some theories on using boundary friction to reorder objects within a triangular and square workspace. Finally, some new tools are presented in this chapter that simply experiments and demonstrations of this variety.

Bibliography

[1] V. M. Baez, A. Shah, S. Akinwande, N. H. Jafari, and A. T. Becker, "Assessment of soil strength using a robotically deployed and retrieved penetrometer," in *2020 IEEE/RSJ International Conference on Intelligent Robots and Systems (IROS)*. IEEE, 2020, p. tbd.

[2] V. M. Baez, S. Poyrekar, M. Ibarra, Y. Haikal, N. H. Jafari, and A. T. Becker, "Wetland soil strength tester and core sampler using a drone," in *2021 IEEE International Conference on Robotics and Automation (ICRA)*. IEEE, 2021, p. tbd.

[3] A. Schmidt, V. M. Baez, A. T. Becker, and S. P. Fekete, "Coordinated particle relocation using finite static friction with boundary walls," *IEEE Robotics and Automation Letters*, vol. 5, no. 2, pp. 985–992, 2020.

[4] R. A. Moan, V. M. Baez, A. T. Becker, and J. M. O'Kane, "Aggregation and localization of simple robots in curved environments," in *2020 IEEE International Conference on Robotics and Automation (ICRA)*, 2020, pp. 165–171.

[5] J. Leclerc, H. Zhao, D. Z. Bao, A. T. Becker, M. Ghosn, and D. J. Shah, "Agile 3d-navigation of a helical magnetic swimmer," in *2020 IEEE International Conference on Robotics and Automation (ICRA)*, 2020, pp. 7638–7644.

[6] J. Leclerc, H. Zhao, D. Bao, and A. T. Becker, "In vitro design investigation of a rotating helical magnetic swimmer for combined 3-d navigation and blood clot removal," *IEEE Transactions on Robotics*, vol. 36, no. 3, pp. 975–982, 2020.

[7] D. Eguren, T. P. Luu, A. Kilicarslan, S. Akinwande, M. Zanovello, A. Arunkumar, J. Gorges, and J. L. Contreras-Vidal, "Development of a pediatric lower-extremity gait

system," in *2017 International Symposium on Wearable Robotics and Rehabilitation (WeRob)*, 2017, pp. 1–1.

[8] A. Bhattacharjee, Y. Lu, A. T. Becker, and M. J. Kim, "Magnetically-controlled modular cubes with reconfigurable self-assembly and disassembly and programmable patterns," *Under Review*, 2021.

[9] Y. Lu, A. Bhattacharjee, D. Biediger, M. J. Kim, and A. T. Becker, "Enumeration of polyominoes & polycubes composed of magnetic cubes," in *Under Review*, 2021.

[10] E. Niehs, A. Schmidt, C. Scheffer, D. E. Biediger, M. Yannuzzi, B. Jenett, A. Abdel-Rahman, K. C. Cheung, A. T. Becker, and S. P. Fekete, "Recognition and reconfiguration of lattice-based cellular structures by simple robots," in *2020 IEEE International Conference on Robotics and Automation (ICRA)*, 2020, pp. 8252–8259.

[11] A. Nguyen, D. Krupke, M. Burbage, S. Bhatnagar, S. P. Fekete, and A. T. Becker, "Using a uav for destructive surveys of mosquito population," in *2018 IEEE International Conference on Robotics and Automation (ICRA)*, 2018, pp. 7812–7819.

[12] D. Biediger, A. Mahadev, and A. T. Becker, "Investigating the survivability of drone swarms with flocking and swarming flight patterns using virtual reality," in *2019 IEEE 15th International Conference on Automation Science and Engineering (CASE)*, 2019, pp. 1718–1723.

[13] C. Wigand, C. T. Roman, E. Davey, M. Stolt, R. Johnson, A. Hanson, E. B. Watson, S. B. Moran, D. R. Cahoon, J. C. Lynch, and P. Rafferty, "Below the disappearing marshes of an urban estuary: historic nitrogen trends and soil structure," *Ecological Applications*, vol. 24, no. 4, pp. 633–649, 2014.

[14] T. M. Twohig and M. H. Stolt, "Soils-based rapid assessment for quantifying changes in salt marsh condition as a result of hydrologic alteration," *Wetlands*, vol. 31, no. 5, p. 955, 2011.

[15] P. Robertson and K. Cabal, *Guide to Cone Penetration Testing For Geotechnical Engineering*, 6th ed. Signal Hill, California: Gregg Drilling & Testing, Inc., 2015.

[16] M. B. Mumtaz, "Investigation of pore pressures during high-velocity impact by a free fall penetrometer," Ph.D. dissertation, Virginia Tech, 2018.

[17] M. Mumtaz, N. Stark, and S. Brizzolara, "Pore pressure measurements using a portable free fall penetrometer," in *Cone Penetration Testing 2018: Proceedings of the 4th International Symposium on Cone Penetration Testing (CPT'18), 21-22 June, 2018, Delft, The Netherlands.* CRC Press, 2018, p. 461.

[18] N. Stark, B. Radosavljevic, B. Quinn, and H. Lantuit, "Application of portable free-fall penetrometer for geotechnical investigation of arctic nearshore zone," *Canadian Geotechnical Journal*, vol. 54, no. 1, pp. 31–46, 2017.

[19] G. K. Mulukutla, L. C. Huff, J. S. Melton, K. C. Baldwin, and L. A. Mayer, "Sediment identification using free fall penetrometer acceleration-time histories," *Marine Geophysical Research*, vol. 32, no. 3, pp. 397–411, 2011.

[20] M. Nazem, J. P. Carter, D. W. Airey, and S. Chow, "Dynamic analysis of a smooth penetrometer free-falling into uniform clay," *Géotechnique*, vol. 62, no. 10, pp. 893–905, 2012.

[21] D. White, C. O'Loughlin, N. Stark, and S. H. Chow, "Free fall penetrometer tests in sand: Determining the equivalent static resistance," in *Cone penetration testing 2018:*

Proceedings of the 4th international symposium on cone penetration testing. CRC Press Boca Raton, FL, USA, 2018, pp. 695–701.

[22] P. L. Wiberg, S. Fagherazzi, and M. L. Kirwan, "Improving predictions of salt marsh evolution through better integration of data and models," *Annual review of marine science*, vol. 12, pp. 389–413, 2020.

[23] S. Fagherazzi, G. Mariotti, N. Leonardi, A. Canestrelli, W. Nardin, and W. S. Kearney, "Salt marsh dynamics in a period of accelerated sea level rise," *Journal of Geophysical Research: Earth Surface*, vol. 125, no. 8, p. e2019JF005200, 2020.

[24] G. Mariotti, T. Elsey-Quirk, G. Bruno, and K. Valentine, "Mud-associated organic matter and its direct and indirect role in marsh organic matter accumulation and vertical accretion," *Limnology and Oceanography*, 2020.

[25] R. R. Lane, S. K. Mack, J. W. Day, R. D. DeLaune, M. J. Madison, and P. R. Precht, "Fate of soil organic carbon during wetland loss," *Wetlands*, vol. 36, no. 6, pp. 1167–1181, 2016.

[26] J. T. Morris, D. C. Barber, J. C. Callaway, R. Chambers, S. C. Hagen, C. S. Hopkinson, B. J. Johnson, P. Megonigal, S. C. Neubauer, and T. Troxler, "Contributions of organic and inorganic matter to sediment volume and accretion in tidal wetlands at steady state," *Earth's future*, vol. 4, no. 4, pp. 110–121, 2016.

[27] A. Farinha, R. Zufferey, P. Zheng, S. F. Armanini, and M. Kovac, "Unmanned aerial sensor placement for cluttered environments," *IEEE Robotics and Automation Letters*, vol. 5, no. 4, pp. 6623–6630, 2020.

[28] S. K. Sudarshan, L. Huang, C. Li, R. Stewart, and A. T. Becker, "Seismic surveying with drone-mounted geophones," in *2016 IEEE International Conference on Automation Science and Engineering (CASE)*. IEEE, 2016, pp. 1354–1359.

[29] R. Stewart, L. Chang, S. Sudarshan, A. Becker, and L. Huang, "An unmanned aerial vehicle with vibration sensing ability (seismic drone)," in *SEG Technical Program Expanded Abstracts 2016*. Society of Exploration Geophysicists, 2016, pp. 225–229.

[30] S. K. Sudarshan, V. Montano, A. Nguyen, M. McClimans, L. Chang, R. R. Stewart, and A. T. Becker, "A heterogeneous robotics team for large-scale seismic sensing," *IEEE Robotics and Automation Letters*, vol. 2, no. 3, pp. 1328–1335, 2017.

[31] D. Castendyk, J. Voorhis, and B. Kucera, "A validated method for pit lake water sampling using aerial drones and sampling devices," *Mine Water and the Environment*, pp. 1–15, 2020.

[32] J.-P. Ore, S. Elbaum, A. Burgin, and C. Detweiler, "Autonomous aerial water sampling," *Journal of Field Robotics*, vol. 32, no. 8, pp. 1095–1113, 2015.

[33] M. Schwarzbach, M. Laiacker, M. Mulero-Pázmány, and K. Kondak, "Remote water sampling using flying robots," in *2014 International Conference on Unmanned Aircraft Systems (ICUAS)*. IEEE, 2014, pp. 72–76.

[34] A. Terada, Y. Morita, T. Hashimoto, T. Mori, T. Ohba, M. Yaguchi, and W. Kanda, "Water sampling using a drone at yugama crater lake, kusatsu-shirane volcano, japan," *Earth, Planets and Space*, vol. 70, no. 1, pp. 1–9, 2018.

[35] F. D'Arcy, J. Stix, J. de Moor, J. Rüdiger, J. Diaz, A. Alan, and E. Corrales, "Drones swoop in to measure gas belched from volcanoes," *EOS*, 2018. [Online]. Available: https://eos.org/science-updates/drones-swoop-in-to-measure-gas-belched-from-volcanoes

[36] D. F. Carlson, J. Pasma, M. E. Jacobsen, M. H. Hansen, S. Thomsen, J. P. Lillethorup, F. S. Tirsgaard, A. Flytkjær, C. Melvad, K. Laufer, L. C. Lund-Hansen, L. Meire, and S. Rysgaard, "Retrieval of ice samples using the ice drone," *Frontiers in Earth Science*, vol. 7, p. 287, 2019. [Online]. Available: https://www.frontiersin.org/article/10.3389/feart.2019.00287

[37] Y. Sun, A. Plowcha, M. Nail, S. Elbaum, B. Terry, and C. Detweiler, "Unmanned aerial auger for underground sensor installation," in *2018 IEEE/RSJ International Conference on Intelligent Robots and Systems (IROS)*. IEEE, 2018, pp. 1374–1381.

[38] A. Plowcha, Y. Sun, C. Detweiler, and J. Bradley, "Predicting digging success for unmanned aircraft system sensor emplacement," in *International Symposium on Experimental Robotics*. Springer, 2018, pp. 153–164.

[39] M. C. Hoang, V. H. Le, J. Kim, E. Choi, B. Kang, J.-O. Park, and C.-S. Kim, "Untethered robotic motion and rotating blade mechanism for actively locomotive biopsy capsule endoscope," *IEEE Access*, vol. 7, pp. 93 364–93 374, 2019.

[40] X.-Z. Chen, M. Hoop, F. Mushtaq, E. Siringil, C. Hu, B. J. Nelson, and S. Pané, "Recent developments in magnetically driven micro- and nanorobots," *Applied materials today*, vol. 9, pp. 37–48, 2017.

[41] J. Garcia, S. Soto, A. Sultana, J. Leclerc, M. Pan, and A. T. Becker, "Underwater robot localization using magnetic induction: Noise modeling and hardware validation," in *Global Oceans 2020: Singapore – U.S. Gulf Coast*, 2020, pp. 1–5.

[42] A. Becker, E. D. Demaine, S. P. Fekete, and J. McLurkin, "Particle computation: Designing worlds to control robot swarms with only global signals," in *2014 IEEE International Conference on Robotics and Automation (ICRA)*. IEEE, 2014, pp. 6751–6756.

[43] A. T. Becker, E. D. Demaine, S. P. Fekete, J. Lonsford, and R. Morris-Wright, "Particle computation: complexity, algorithms, and logic," *Natural Computing*, vol. 18, no. 1, pp. 181–201, 2019.